

KSZ Velocity Reconstruction with ACT and DESI-LS using a Tomographic QML Power Spectrum Estimator

Anderson Lai ¹, Yurii Kvasiuk ¹, and Moritz Münchmeyer ^{1,2}

¹Department of Physics, University of Wisconsin-Madison, Madison, WI 53706, USA

²NSF-Simons AI Institute for the Sky (SkAI), Chicago, IL 60611, USA

June 30, 2025

Abstract

We perform kinetic Sunyaev-Zel'dovich (kSZ) velocity reconstruction on data from ACT DR6 and DESI-LS DR9. To estimate the cross-power between kSZ velocity reconstruction and galaxy density, we make use of a novel quadratic maximum likelihood QML power spectrum estimator implementation in red-shift binned spherical coordinates. We find a detection of the kSZ signal from the cross-correlation between the estimated velocity field and the large-scale galaxy field of 11.7σ . We estimate an amplitude $A = 0.39 \pm 0.04$ of the kSZ signal with respect to a halo model prediction, possibly indicating a high feedback in massive halos, in agreement with previous studies. Our result demonstrates the feasibility of an optimal QML pipeline at the resolution required for this analysis, and will be a powerful tool for kSZ cosmology with upcoming high-resolution surveys.

Contents

1	Introduction	2
2	Analysis Pipeline	3
2.1	Data set	3
2.1.1	ACT DR6 temperature maps	3
2.1.2	DESI LS DR9 extended LRG sample and calibration	4
2.2	Quadratic Estimator and Noise Covariance Estimation	6
2.3	Velocity Map Coadding	9
2.4	Quadratic Maximum Likelihood Cross-Power Spectrum Estimator	10
2.5	Fiducial Powers	11
2.6	Cross-Correlation Signal-to-Noise	13
3	Results: kSZ Velocity Reconstruction and Cross-Correlation	15
3.1	kSZ velocity field reconstruction with ACT and DESI-LS	15
3.2	Velocity-Galaxy Cross-Power Spectrum	16
4	Results: Linear Velocity Map Reconstruction from Galaxy Over-Density maps	19
4.1	Linear reconstruction	20
4.2	Result on DESI-LS	20
5	Conclusion	21
A	Imaging Calibration for the DESI LRG Extended Sample	26
B	Fisher Forecast for the QML Estimator	26
C	Definition of the SNR as a Significance of the Rejection of the Null Hypothesis	27
D	Rescaling of the kSZ Estimator under Fiducial Power $C_{g\tau}$	29
E	Bandpowering Scheme for Velocity-Galaxy Cross-Powers	31

arXiv:2506.21684v1 [astro-ph.CO] 26 Jun 2025

F	Linear Estimator of the Velocity Field from Galaxies	31
F.1	Construction of the Velocity Estimator from Maximizing the Joint Probability $\mathcal{P}(v_r^{\text{true}}, \delta_g^{\text{obs}})$. . .	31
F.2	Validating the Velocity Reconstruction on Simulations	33
G	A Comparison with Pseudo-C_ℓ	33
H	All Estimated 20×20 Bin Galaxy-Velocity Cross-Power Spectra C_ℓ^{gv}	33

1 Introduction

Current and upcoming CMB experiments measure CMB secondary anisotropies with unprecedented precision, making them a powerful probe of astrophysics and cosmology. On intermediate scales these anisotropies are dominated by CMB lensing [31]. On even smaller scales, the dominant contribution to the CMB blackbody anisotropy is the kinetic Sunyaev-Zeldovich (kSZ) effect [45], the re-scattering of CMB photons on the bulk movement of free electrons in the universe. The kSZ has been detected by cross-correlation with galaxies in [20, 40, 42, 15, 22, 13, 43]. The strongest detection to date comes from the recent paper [18] which found 13σ using ACT data in cross-correlation with photometric galaxy data (DESI-LS). However, for upcoming experiments the expected signal-to-noise (SNR) is much higher, for example Simons Observatory (SO) and Rubin Observatory will reach $\text{SNR} \simeq 200$ [44]. The kSZ has both astrophysical and cosmological applications. In astrophysics, the kSZ has been used to measure the gas profile of galaxy clusters [24, 42, 43], which contains information about astrophysical galactic processes such as AGN feedback [2]. However the kSZ is also a powerful probe of cosmology (see e.g. [14, 21, 3]) and can be used to constrain for example modified gravity [34, 4], and neutrino masses [35]. Recent kSZ analyses using ACT data with other methods than the one presented here include [43, 32, 7, 1, 19].

In the present work we apply a method called *kSZ velocity reconstruction*, which uses the kSZ to reconstruct the large-scale velocity field of the universe. This velocity field could then be used to probe cosmology, in a similar way to the CMB lensing potential (both methods probe the total matter distribution on large scales), but we defer cosmological parameter analysis to future work. kSZ velocity reconstruction was first proposed in [16] (there called remote dipole reconstruction) and further developed in [44, 8]. kSZ velocity reconstruction has been applied to data for the first time in 2024 in several different analyses using various data combinations [33, 6, 30, 27]. References [6, 27] used data from Planck and unWISE to constrain the optical depth bias as well as primordial non-Gaussianity, while [33, 30] used ACT data in combination with DESI-LS and SDSS to detect the kSZ signal at 3.8σ and 7.2σ , respectively. A number of authors have proposed possible applications of the kSZ velocity reconstruction method to constrain fundamental parameters of the universe, including modified gravity [39], isocurvature perturbations [26] and statistical anisotropies [9]. A perhaps particularly promising application is the measurement of the local non-Gaussianity parameter f_{NL} , which was proposed in [36]. The kSZ velocity reconstruction method was also studied with simulations in [10, 17].

In this work, we apply kSZ velocity reconstruction to ACT DR6 data and photometric galaxy data from DESI Legacy Survey DR9. Two previous works have applied this method to ACT data [33, 30]. Our analysis differs from these works in the following ways:

- We use the DESI Legacy Survey (DESI-LS) both to construct the quadratic velocity estimator (which uses the small-scale galaxy distribution), and to cross-correlate the large-scale kSZ velocity reconstruction with the large-scale galaxy field. Contrary, previous analyses used spectroscopic galaxy data from SDSS to generate a large-scale velocity template from the galaxy field for cross-correlation with the kSZ velocity reconstruction. We also use finer redshift bins than the ACT DR6 analysis in [33], which allows us to increase the SNR.
- We develop a novel implementation of the optimal quadratic maximum likelihood (QML) power spectrum estimator, instead of using the common but suboptimal pseudo- C_ℓ method. This estimator uses a pixel-wise covariance matrix, which we make computationally tractable for the required large-scale analysis ($\ell_{\text{max}} = 60$, HEALPix NSIDE=32 and 20 redshift bins for both fields). More details about our novel QML estimator will be provided in an upcoming companion paper. We find that this estimator almost doubles the signal-to-noise compared to the more standard pseudo- C_ℓ approach with identical analysis choices. An interesting aspect of our implementation is that we can calculate the full covariance matrix (including mask effects) analytically, rather than having to run a large ensemble of (Gaussian) Monte Carlo simulations.

In combination these improvements allow us to reach an SNR of 11.7σ , which is the highest SNR obtained with this method to date (and equal to [25] published at the same time). While in the present paper we only reconstruct the velocity field and do not perform a cosmological parameter analysis, our novel QML pipeline is well suited for an optimal cosmology analysis on large-scales, which we will provide in followup work.

This paper is similar in scope to [25], submitted to arXiv at the same time, which also does kSZ velocity reconstruction with $\text{ACT} \times (\text{DESILS LRGs})$. Our pipeline is 2+1 dimensional, while [25] has a 3-dimensional cartesian representation of the data. We also make different analysis choices. In particular, [25] uses only the DESI-LS Northern Galactic Hemisphere area to reduce image systematics (while still retaining a large part of the SNR). The two papers are substantially different in their pipeline and analysis choices but reach very similar results in terms of SNR and kSZ velocity bias $b_v \sim 0.4$. The paper [25] also includes a measurement of local primordial non-Gaussianity, which we defer to future work.

The paper is organized as follows. In Sec. 2 we describe the input data and the analysis pipeline, including the novel QML estimator implementation. In Sec. 3 we apply the pipeline to data and provide a number of consistency checks. In Sec. 4 we make a linear reconstruction of the velocity field from DESI-LS, which we can then use to compare to the kSZ-derived velocity reconstruction. We conclude in Sec. 5. A number of appendices provide more details for our analysis.

2 Analysis Pipeline

In this section we describe the data set, review the quadratic estimator velocity reconstruction, describe our novel QML power spectrum implementation, and evaluate signal and noise covariance matrices.

2.1 Data set

2.1.1 ACT DR6 temperature maps

We use the coadded temperature maps from ACT Data Release 6 (DR6), which are the latest dataset available to the public [38]. The ACT DR6 maps preserve a relatively large footprint ($\approx 43\%$), while offering a lower noise level beyond $\ell > 1000$ compared to the Planck satellite, which has a more complete sky coverage. The kSZ reconstruction is performed on the 90 GHz and 150 GHz channel maps, which have the least amount of contamination from the foregrounds such as the tSZ effect and the cosmic infrared background (CIB). We

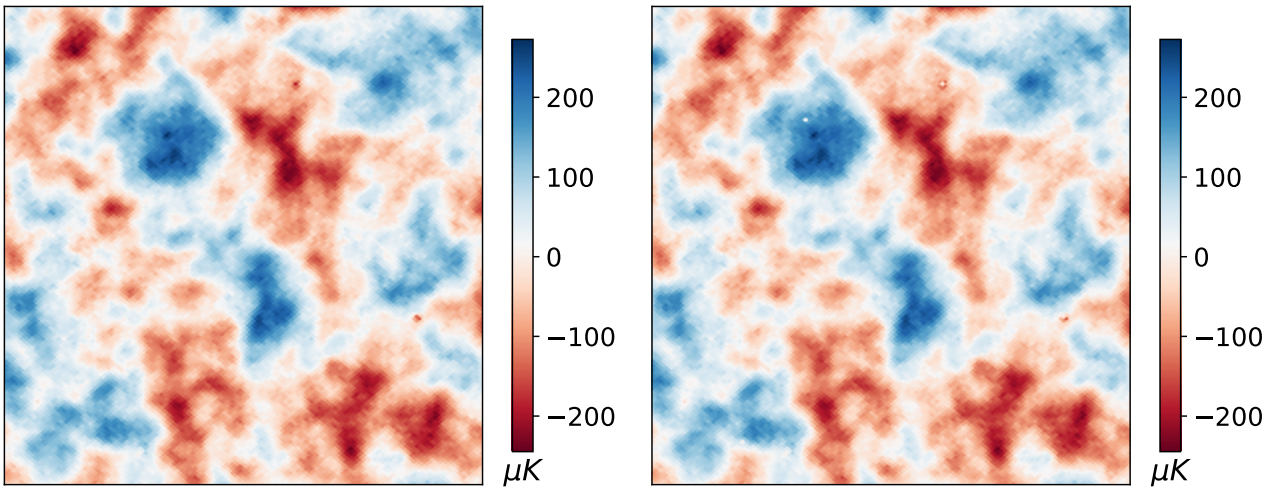


Figure 1: A figure illustrating the ACT DR5 90 GHz temperature map before and after the SZ cluster masking over a $4^\circ \times 4^\circ$ region. The SZ clusters behave as dense cold spots at the 90 GHz channel, which can be seen from the middle top region and bottom left region of the left plot. The SZ clusters are then masked according to the catalog from [23] as shown in the right figure, such that the center of the SZ clusters are replaced by zero before deconvolving the maps. The SZ cluster mask could potentially remove anisotropic foregrounds that may bias the kSZ reconstruction, but we find only a negligible impact in our analysis below.

prepare the temperature maps on individual frequencies. To avoid any bright point sources and false photometry that may induce excessive power at small scale, we start with source-free temperature maps. A SZ cluster mask with $\text{SNR} > 5$ is generated from the catalog given in [23] and applied to the temperature maps to remove anisotropic tSZ foreground. Fig. 1 illustrates a square region from the 90 GHz temperature map before and after the tSZ masking. The maps are then deconvolved using the equivalent beam profile as prescribed in [37] and are overlaid with a sky mask from the DR6 internal-linear combination analysis [12] to remove regions that are nearby the galactic plane. The left plot in Fig. 2 shows the superposed mask that we use for the temperature maps, the remaining sky coverage is approximately 25.7%. We present the temperature power spectrum \tilde{C}_ℓ^{TT} 's

computed from the processed temperature maps in the right plot of Fig. 2. The source-free temperature maps, equivalent beam profiles, SZ cluster catalog and mask are all publicly available from the ACT repository.

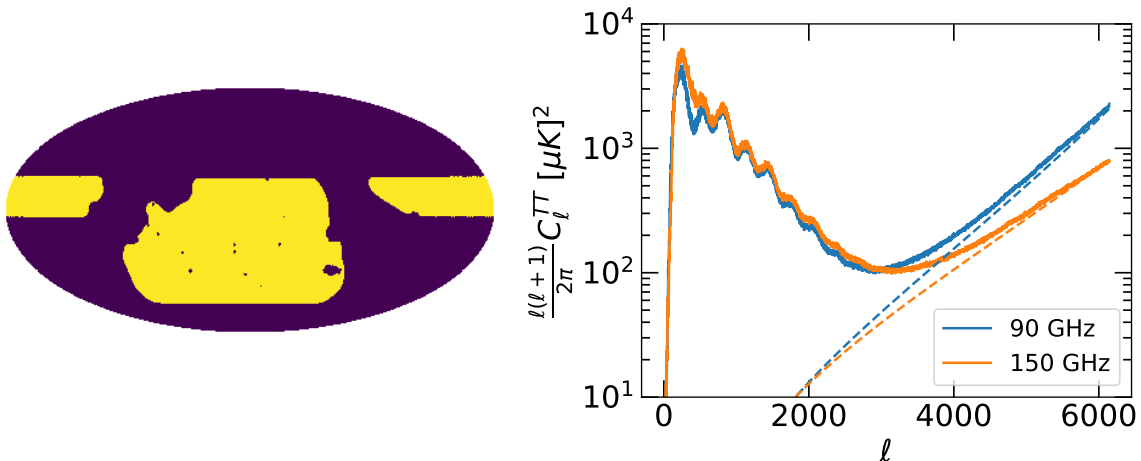


Figure 2: Left: A binary mask created from the apodized DR6 NILC analysis mask in [12]. The mask has been superposed with the tSZ mask described in the main test and is not clearly seen in the figure due to scale of presentation. Right: The observed temperature power spectrum \tilde{C}_ℓ^{TT} calculated from the preprocessed, coadded temperature maps. The blue (orange) curve corresponds to the 90 (150) GHz channel. The temperature power spectrum is presented in the unit of $(\mu\text{K})^2$. The red and green dashed curves are included in the plot to illustrate the asymptotic behavior of \tilde{C}_ℓ^{TT} at large scale, due to beam deconvolution.

2.1.2 DESI LS DR9 extended LRG sample and calibration

We use the DESI LS (Legacy Survey) DR9 extended LRG (Luminous Red Galaxy) sample from [50, 49] to compute the quadratic kSZ velocity estimator as well as the velocity-galaxy cross-power C_ℓ^{vg} . The full DR9 extended LRG catalog has a footprint of nearly 44% of the full sky and contains approximately 3.4×10^7 objects. This number reduces to 2.8×10^7 after applying the veto mask to remove objects with false photometry or with invalid selection criteria. This sample doubles the number of galaxies that was used in [33], hence providing a lower galaxy shot noise N_ℓ^{gg} and improving the quality of the kSZ reconstruction.

The filtered catalog is divided into 20 redshift bins, ranging from $z = 0.4$ to $z = 1.1$ at constant intervals of $\Delta z = 0.035$. To account for the photo- z error, we use a similar procedure as in [33] by convolving each redshift bin with a Gaussian kernel of width equal to $\sigma_z(1+z)$, where $\sigma_z = 0.027$ is the photo- z error reported in [49] for the southern sky sample. We note that the photo- z error in the northern sky is different from the southern sky, the smaller between the two number is picked to represent the general photo- z for this analysis.

Fig. 3 presents the distribution of galaxy number density $n_g^\alpha(z)$ a selection of the redshift bins, with photo- z error included. There are significant overlaps among the redshift bins, as the size of the redshift bins is now comparable to the photo- z error. Therefore, a full correlation of all redshift bins has to be considered in the SNR analysis. From the distribution of the galaxy number density, we introduce the normalized window function:

$$W^\alpha(z) = \frac{n_g^\alpha(z)}{\int dz n_g^\alpha(z)}, \quad (1)$$

for each redshift bin α . The window functions are used to incorporate the photo- z effect into the calculation of theoretical power spectrum.

We project the redshift-binned galaxy catalog onto 2D maps with `Healpix` format to generate a set of galaxy density maps. The galaxy density maps are constructed in three different resolutions $N_{\text{side}} = 32, 256, 4096$ throughout the analysis. The QML pipeline implemented for the SNR calculation (see Sec. 2.4) requires galaxy density maps with accurate large-scale behavior. Therefore, we start by calibrating the galaxy density maps on a smaller $N_{\text{side}} = 256$. The calibrated maps are then further downgraded to $N_{\text{side}} = 32$ and used as inputs for the QML pipeline. On the other hand, the kSZ quadratic estimator (see Sec. 2.2) relies on galaxy density maps with small-scale features of $\ell > 1000$. Therefore, we chose $N_{\text{side}} = 4096$ as the baseline resolution for the kSZ reconstruction.

The calibrated galaxy overdensity maps δ_g^α are computed on $N_{\text{side}} = 256$ using the equation below:

$$\delta_g^\alpha(\hat{n}) = \frac{n_g^\alpha(\hat{n})}{n_{\text{expected}}^\alpha(\hat{n})} D^\alpha - 1, \quad (2)$$

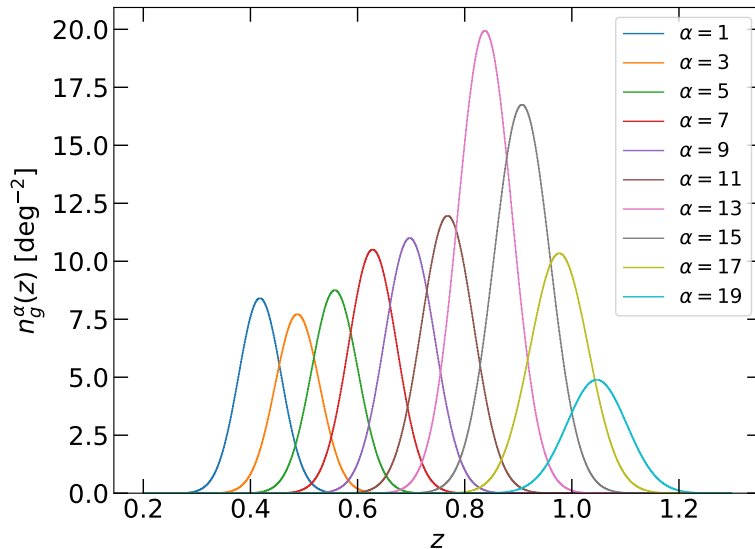


Figure 3: The redshift distribution of the 20 galaxy tomographic bins in an interval of 2 bins, objects between $z = 0.4$ to $z = 1.1$ are used in this analysis. The redshift bins presented in this figure have been convolved with the photo- z error and have not been normalized.

the expected galaxy density counts $n_{\text{expected}}^\alpha(\hat{n})$ are generated from a random catalog of a total 1.33×10^9 random points provided by [49] on the same N_{side} and the normalization factor

$$D^\alpha = \frac{\sum_{\hat{n}} n_{\text{expected}}^\alpha}{\sum_{\hat{n}} n_g^\alpha}, \quad (3)$$

is to account for the different number of galaxies in the data and the random catalog. Following [50, 41], we obtain the expected galaxy density by creating a linear model of 12 parameters:

$$n_{\text{expected}}^\alpha(\hat{n}) = c_0^\alpha + \sum_{i=1}^{11} \sum_{j=1}^{n_{\text{rand}}} c_i^\alpha s_j^i(\hat{n}), \quad (4)$$

here every index i represents a systematic associated to the random catalog and every index j represents a random that is projected to the pixel along direction \hat{n} with value s_j^i , the modeling coefficients c_0, c_i depends on the redshift bin α but not the position of the pixel \hat{n} . n_{rand} is the galaxy density map from the random catalog, it varies with the location of the pixels but not the redshift. A regression model is then created by finding the best-fit values of c_0^α, c_i^α through minimizing the chi-square value for each redshift bin α :

$$\chi^{\alpha 2} = |n_{\text{expected}}^\alpha - n_g^\alpha|^2 \quad (5)$$

Once the calibrated galaxy overdensity maps are obtained, they are downgraded from $N_{\text{side}} = 256$ to $N_{\text{side}} = 32$ to be compatible with the input resolution of the QML estimators. The downgrading is performed by first converting the galaxy overdensities into spherical harmonic coefficients, modes beyond $\ell = 3 \times N_{\text{side}} - 1 = 95$ are then filtered. Finally, the spherical harmonic modes are transformed back to the pixel space. Comparing to the pixel-space averaging method, this procedure prevents the contamination from modes beyond $3 \times N_{\text{side}} - 1$. More details about calibration are provided in App. A.

Fig. 5 displays the 20-bin galaxy autopowers, which are further averaged into four larger redshift intervals. To illustrate the difference in galaxy autopowers before and after calibration up to an intermediate scale $\ell = 100$, we compute the pseudo- C_ℓ power spectrum from the $N_{\text{side}} = 256$ maps using the Python package `PyMaster`. We then average the galaxy autopowers within the interval by taking a weighted sum of them, using the inverse of their galaxy shot noise $N^{gg,\alpha}$ as their weights. The orange curves show the power spectrum calculated from galaxy overdensity maps with just a random catalog subtraction. In contrast to the orange curves, the blue curves are calibrated with imaging systematics, which reduces the excess powers on large scale $\ell < 20$ across all redshift intervals. However, we note that the imaging calibration adopted in this analysis does not completely remove such an excess of large-scale power. The residual excess can potentially be removed by employing a regression model with nonlinear terms or including other imaging systematics, we defer the investigation to future work. The imaging calibration becomes almost negligible at $\ell > 50$ and the two galaxy autopowers converge. For reference, fiducial galaxy autopowers are included in the plot as the red and purple curves. It

can be observed that the RSD effect introduces extra power to large scales, which is non-negligible and has to be accounted for yielding a better fit to the data.

We also present the bandpowered QML estimates for the 20 galaxy autopowers in Fig. 6 over a smaller range of modes $7 < \ell < 60$. The $N_{\text{side}} = 32$, calibrated maps are used for the QML estimators. At $\ell > 20$, most of the QML estimates align with the theory within the 1-sigma region. However, the large-scale excess at some redshift bins ($\alpha = 12, 13$) and at the lowest bandpower ($\ell = 7 - 12$) remains prominent, which is again due to incomplete removal of the systematics.

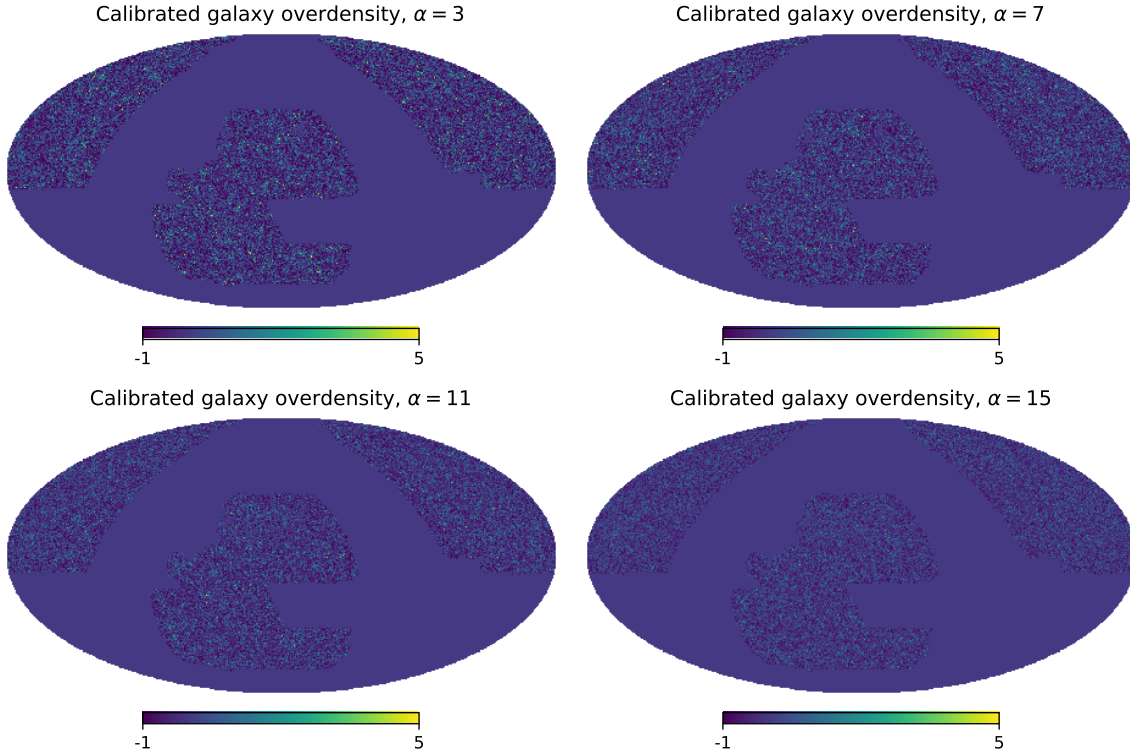


Figure 4: A selection of DESI LRG galaxy overdensity map used in this analysis. The overdensity maps are calibrated using a regression model of 11 imaging systematic maps over the DESI footprint. The maximum overdensity is set at 5 for the purpose of illustration.

2.2 Quadratic Estimator and Noise Covariance Estimation

We give a brief summary on the binned-2D quadratic velocity field estimator used for the kSZ reconstruction in this analysis.¹ The velocity modes at a particular redshift bin $\hat{v}_{\ell m}^\alpha$ can be estimated from a quadratic estimator of CMB anisotropy $a_{\ell m}$ and galaxy overdensity from the same redshift bin $\delta_{g, \ell m}^\alpha$:

$$\hat{v}_{\ell m}^\alpha = \sum_{l_1 m_1, l_2 m_2} W_{l m, l_1 m_1 l_2 m_2} a_{l_1 m_1} \delta_{g, l_2 m_2}^\alpha. \quad (6)$$

Here $W_{l m, l_1 m_1 l_2 m_2}$ is a window function to be determined through the constraint of an unbiased estimator $\langle \hat{v}_{\ell m}^\alpha \rangle = v_{\ell m}^\alpha$ and minimum variance $\langle (\hat{v}_{\ell m}^\alpha - v_{\ell m}^\alpha)^2 \rangle$. As described in [16, 44, 29, 6], by treating $a_{\ell m}$ and $\delta_{g, \ell m}^\alpha$ to be Gaussian to the leading order and by working in the regime where the kSZ signal is dominated by the small-scale power, the window function can be solved using the Lagrange multiplier, leading to the following result:

$$\hat{v}_{\ell m}^\alpha = N_\ell^{vv, \alpha} \sum_{\ell_1, \ell_2, m_1, m_2} (-1)^{m+1} \Gamma_{\ell_1 \ell_2 \ell}^\alpha \begin{pmatrix} \ell_1 & \ell_2 & \ell \\ m_1 & m_2 & -m \end{pmatrix} \frac{a_{\ell_1 m_1} \delta_{g, \ell_2 m_2}^\alpha}{C_{\ell_1}^{TT} C_{\ell_2}^{gg, \alpha}}, \quad (7)$$

where $C_{\ell_1}^{TT}$ is the full-sky CMB autopower, $C_{\ell_2}^{gg, \alpha}$ is the full-sky galaxy power spectrum at redshift bin α , both include signal and noise. Wigner 3-j symbol was used in above expression. The kSZ coefficient $\Gamma_{\ell_1 \ell_2 \ell}^\alpha$ is defined

¹The use of the optimal MAP estimator leads to the improvement in reconstruction only in the case of significantly lower noises in the CMB and galaxy data[29]

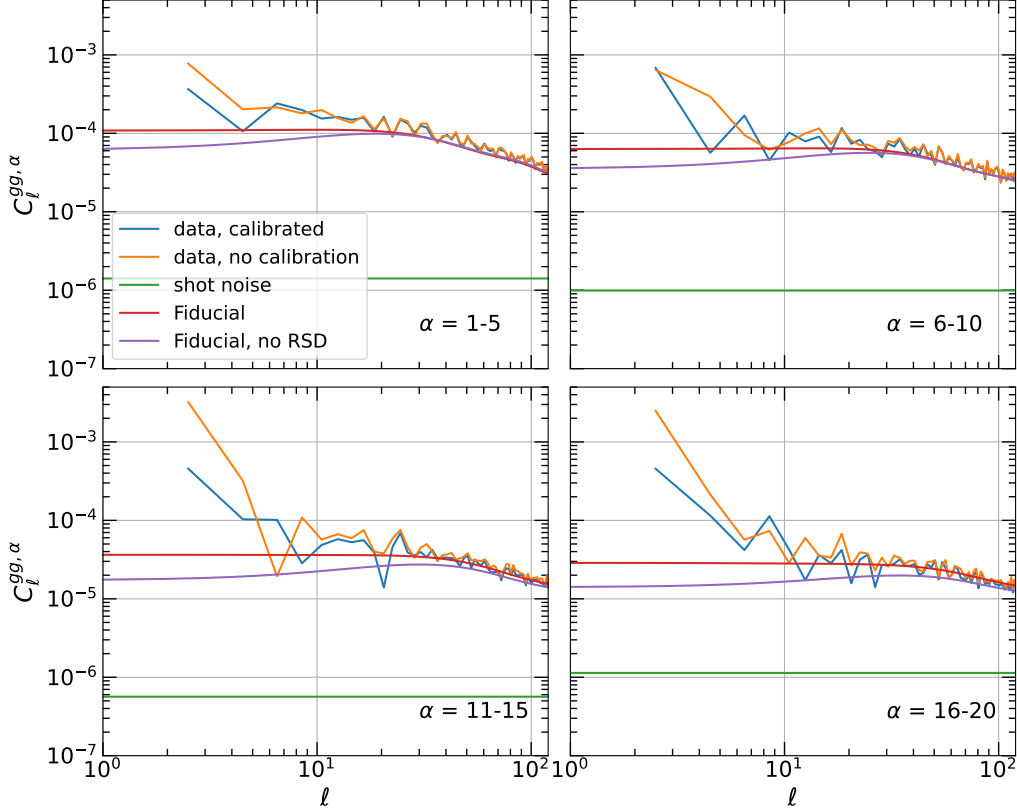


Figure 5: Galaxy autopower spectrum in 4 redshift intervals (consisting of 5 bins), showing the correction on the large-scale galaxy autopower from the imaging calibration. We also show that the RSD contribution to the fiducial power is not negligible. Each plot is obtained by a weighted-average of the pseudo- C_ℓ galaxy autopowers from individual redshift bin $C_\ell^{gg, \alpha}$ within the redshift interval. The fiducial powers are computed using `pycc1`. It is noted that the power spectrum shown in this plot is for illustration and is not used in the analysis below.

as:

$$\Gamma_{\ell_1 \ell_2 \ell}^\alpha = \sqrt{\frac{(2\ell_1 + 1)(2\ell_2 + 1)(2\ell + 1)}{4\pi}} \begin{pmatrix} \ell_1 & \ell_2 & \ell \\ 0 & 0 & 0 \end{pmatrix} C_{\ell_2}^{\tau g, \alpha}, \quad (8)$$

with $C_{\ell_2}^{\tau g, \alpha}$ as the cross power between the electron density and galaxy at redshift bin α . It is noted that Eq. 8 can be expressed and computed in a more compact form by transforming $\hat{v}_{\ell m}$ back to pixel space, such that [6]:

$$v^\alpha(\hat{n}) = -N^{vv, \alpha} a'(\hat{n}) \delta_g'^\alpha(\hat{n}), \quad (9)$$

where we have assumed that the kSZ reconstruction noise $N_\ell^{vv, \alpha}$ can be approximated by its mean across the multipoles $N^{vv, \alpha}$ and the primed variables denotes the pixel space quantity reconstructed from filtered harmonic coefficients. For example:

$$\delta_g'^\alpha(\hat{n}) = \sum_{\ell_2, m_2} \frac{C_{\ell_2}^{\tau g, \alpha}}{C_{\ell_2}^{gg, \alpha}} \delta_{g, \ell_2 m_2}^\alpha Y_{\ell_2, m_2}(\hat{n}), \quad (10)$$

The kSZ reconstruction noise $N_\ell^{vv, \alpha}$ can be obtained through the following expression:

$$\frac{1}{N_\ell^{vv, \alpha}} = \frac{1}{2\ell + 1} \sum_{\ell_1, \ell_2} \frac{(\Gamma_{\ell_1 \ell_2 \ell}^\alpha)^2}{C_{\ell_1}^{TT} C_{\ell_2}^{gg, \alpha}}. \quad (11)$$

In practice, the pixel-space expression Eq. 9 is implemented to estimate the pixel-space velocity fields. We use observed CMB maps and galaxy overdensity maps of resolution $N_{\text{side}} = 4096$, such that the kSZ component in CMB maps can be well captured. A mask in pixel space that accounts for the overlapping footprint between ACT DR6 and DESI LRG survey is applied to the maps, the shape of the overlapping mask is shown in Fig. 7. We also apply a filter in the spherical harmonic space to remove modes beyond $\ell = 10000$. The theoretical reconstruction noise is calculated separately in spherical harmonic space through Eq. 11, we include modes with

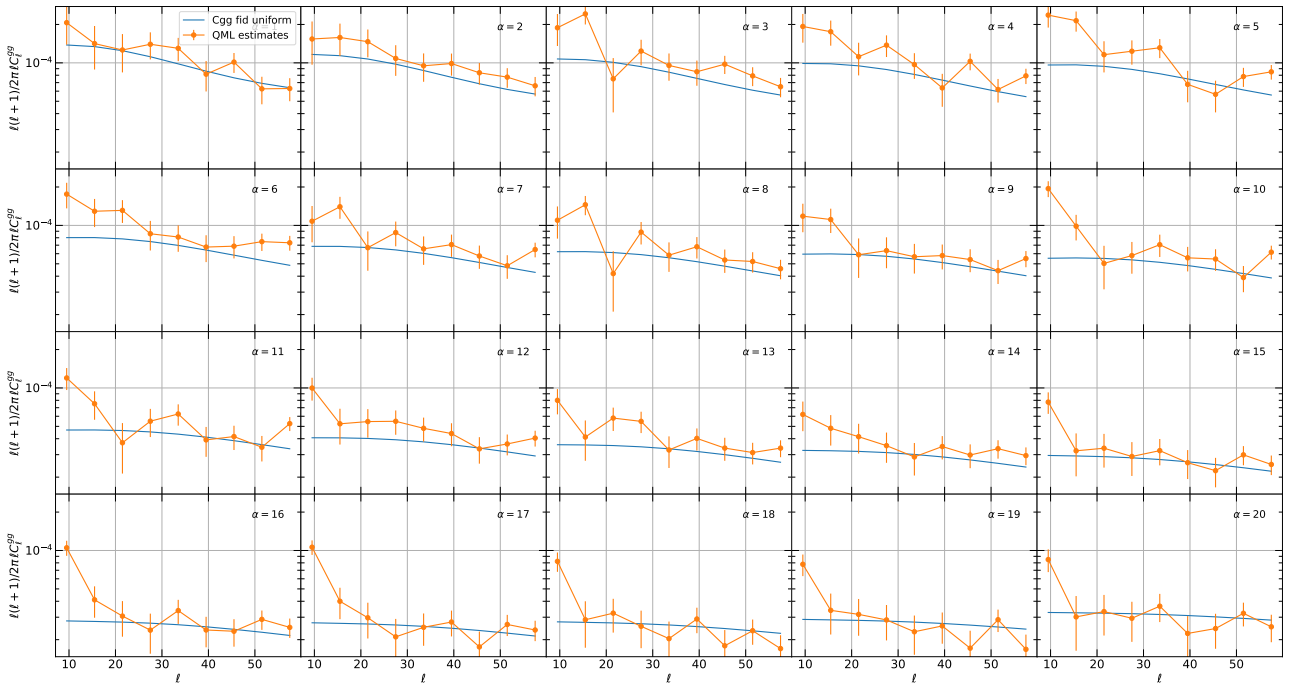


Figure 6: QML estimates on the large-scale Galaxy autopowers $C_\ell^{gg,\alpha}$ between $\ell = 7$ and $\ell = 60$. The estimates are banded in 6 modes per band for better visualization. The errorbars are obtained from the analytic covariance matrix presented in Sec. 3.2. We find that some excess power remains on the largest scales, likely due to calibration and photo-z effects.



Figure 7: The mask constructed from the overlapping region between the ACTDR6 CMB map and DESI-LS DR9 survey. Dots with masked value of zeros show the regions with false photometry, which is removed in the DESI LRG analysis [49]. The mask is applied to pixel-space velocity estimator $\hat{v}(\hat{n})$.

$\ell_1, \ell_2 \in [300, 10000]$ within the summation. Extending the summation of modes below $\ell = 300$ only leads to sub-percent level of changes to the reconstruction noise, hence can be neglected.

To incorporate the observed data in the estimator, we also replaced $\tilde{C}_{\ell_1}^{TT}$ and $C_{\ell_2}^{gg,\alpha}$ with those computed from actual observations $\tilde{C}_{\ell_1}^{TT}$ and $\tilde{C}_{\ell_2}^{gg,\alpha}$. For this analysis, we rescale $\tilde{C}_{\ell_1}^{TT}$ and $\tilde{C}_{\ell_2}^{gg,\alpha}$ computed from the unmasked region by the sky fraction f_{sky} to recover the fullsky power spectrum, which is a good approximation for the kSZ reconstruction. Systematics and foregrounds have to be included in quantities derived from observed CMB maps, such that $\tilde{C}_{\ell_1}^{TT}$ contains survey noise due to beam deconvolution and foreground contamination from the tSZ effect and CIB. This is also true with the input from the galaxy survey, which $\tilde{C}_{\ell_2}^{gg,\alpha}$ carries the shot noise due to the finite number of galaxy counts and photo-z error. In general, the electron-galaxy cross-power $C_{\ell_2}^{\tau g,\alpha}$ should also be obtained from observations. However, there is currently no direct probe onto this quantity. Therefore, $C_{\ell_2}^{\tau g,\alpha}$ is instead calculated from the halo model for this analysis. The uncertainty on the exact amplitude of $C_{\ell_2}^{\tau g,\alpha}$ will induce a linear bias on the overall amplitude of the velocity-galaxy cross-power C_ℓ^{vg} , also known as the optical depth degeneracy [44, 6]. The theoretical calculation of $C_{\ell_2}^{\tau g,\alpha}$ is given in Sec. 2.5

Channel-wise estimator noise covariance. The noise in each channel can be calculated theoretically using Eq. (11), assuming Gaussian fields (corrections to this noise model were studied in [17]). We can also estimate

the noise covariance of the kSZ estimator, in the ℓ range of interest ($\ell < 300$), directly from the data. To do this, we assume that the noise is Gaussian. We also assume that the noise is flat in ℓ , which implies that noise in different pixels is uncorrelated (on large scales, i.e on NSIDE=32). With these assumptions, and knowing that at $\ell > 50$ the estimator is completely noise dominated, we can fit the noise amplitude to the estimator response. Alternatively, one could run simulations to determine the noise level. However, it is not trivial to make the simulations accurate at the small scales required here (including non-Gaussianity), and we believe that bootstrapping the noise covariance from the data is simpler and possibly more reliable. We investigate the potential mismatch between the theoretical reconstruction noise $N_\ell^{vv,\alpha}$ and noise level given by the estimator response. In particular, we compute the pseudo- C_ℓ velocity autopowers C_ℓ^{vv} from the reconstructed, masked velocity maps $\hat{v}(\hat{n})$ and take the mean value between $\ell = 100$ and $\ell = 300$ as the bestfit reconstruction noise $\tilde{N}_\ell^{vv,\alpha}$. We find a mismatch between the theoretical and the estimator noise level, which is displayed in Fig. 8. The ratio of two noise levels, depending on the frequency channel and the redshift bin, can range from 1.1 to 1.7. It is noted that a similar mismatching was also found in other kSZ reconstruction pipeline [33, 6]. To avoid the possibility of underestimating the reconstruction noise, we adopt the best-fit values $\tilde{N}_\ell^{vv,\alpha}$ as our fiducial kSZ noise for the QML estimator. We drop the notation $\tilde{N}_\ell^{vv,\alpha}$ and $N_\ell^{vv,\alpha}$ represents the bestfit reconstruction noise hereafter. We note that the mismatch of the empirical reconstruction noise to the theory prediction is reduced significantly if we cut galaxies with a large photo-z error. We will explore down-weighting of galaxies with large photo-z in future work.

Cross-channel estimator noise covariance. It is noted that the kSZ reconstruction is performed over each CMB maps, leading to individual estimation on the velocity field for each frequency channel. Therefore, one has to account for the kSZ reconstruction noise from the cross-channel velocity autopowers. For the 90 GHz and 150 GHz CMB used in this analysis, we only consider the cross-channel noise $N_{\ell,90 \times 150}^{vv,\alpha}$. Using Eq. 7, one can compute the cross-channel noise as follows:

$$\begin{aligned}
N_{\ell,90 \times 150}^{vv,\alpha} &= \langle \hat{v}_{lm,90}^\alpha \hat{v}_{lm,150}^\alpha \rangle, \\
&= N_{\ell,90}^{vv,\alpha} N_{\ell,150}^{vv,\alpha} \sum_{\ell_1, \ell_2, m_1, m_2} (\Gamma_{\ell_1 \ell_2 \ell}^\alpha)^2 \begin{pmatrix} \ell_1 & \ell_2 & \ell \\ m_1 & m_2 & -m \end{pmatrix}^2 \frac{C_{\ell_1,90 \times 150}^{TT}}{C_{\ell_1,90}^{TT} C_{\ell_1,150}^{TT} C_{\ell_2}^{gg,\alpha}}, \\
&= \frac{N_{\ell,90}^{vv,\alpha} N_{\ell,150}^{vv,\alpha}}{2\ell + 1} \sum_{\ell_1, \ell_2} \frac{(\Gamma_{\ell_1 \ell_2 \ell}^\alpha)^2 C_{\ell_1,90 \times 150}^{TT}}{C_{\ell_1,90}^{TT} C_{\ell_1,150}^{TT} C_{\ell_2}^{gg,\alpha}}.
\end{aligned} \tag{12}$$



Figure 8: Figure comparing the theoretical kSZ reconstruction noise $N_\ell^{vv,\alpha}$ to the best-fit value $\tilde{N}_\ell^{vv,\alpha}$ estimated from the data. The theoretical calculations follows from Eq. 11. While the best-fit estimated noise are obtained from taking the mean value between $\ell = 100$ to $\ell = 300$ in the pseudo- C_ℓ velocity autopowers. The pseudo- C_ℓ power spectrum are computed using PyMaster on $N_{\text{side}} = 128$, mean-subtracted velocity maps.

2.3 Velocity Map Coadding

To maximize the efficiency of the power spectrum estimation from the set of galaxy and velocity maps, we first create a set of coadded velocity maps by defining a linear combination of individual velocity maps from the same redshift bins and with different frequency channels:

$$v_{\text{coadd}}^\alpha = Av_{90}^\alpha + Bv_{150}^\alpha, \tag{13}$$

the velocity maps expressed in pixel space, A and B are coefficients to be determined. Taking the covariance of the maps and using the fact that $\langle v_{90,150,90 \times 150}^\alpha \rangle = 0$ we arrive the expression:

$$C^{vv} + N_{\text{coadd}}^{vv} = (A + B)^2 C^{vv} + A^2 N_{90}^{vv} + B^2 N_{150}^{vv} + 2AB N_{90 \times 150}^{vv}, \quad (14)$$

where C^{vv} is now the pixel covariance matrix and N^{vv} is the coadded noise covariance matrix in the pixel space. Then one can enforce the normalization condition that $A + B = 1$ and minimize the expression with respect to A , giving:

$$A = \frac{N_{150}^{vv} - N_{90 \times 150}^{vv}}{N_{90}^{vv} + N_{150}^{vv} - 2N_{90 \times 150}^{vv}}, \quad B = \frac{N_{90}^{vv} - N_{90 \times 150}^{vv}}{N_{90}^{vv} + N_{150}^{vv} - 2N_{90 \times 150}^{vv}}, \quad (15)$$

and the coadded noise covariance N_{coadd}^{vv} in pixel space can be determined accordingly. In general N^{vv} can be anisotropic, so that the diagonal terms can be different from pixel to pixel. However, under the assumption that the coadded noise behaves as the single-channel noise, which is nearly isotropic, the conversion between pixel space N^{vv} and the power spectrum N_ℓ^{vv} can be simplified:

$$N^{vv} = \frac{12N_{\text{side}}^2}{4\pi} N_\ell^{vv}. \quad (16)$$

For simplicity, we omit the subscript coadd from the velocity field for the remaining text, any quantity associated to the velocity estimation should be understood as the co-added ones.

2.4 Quadratic Maximum Likelihood Cross-Power Spectrum Estimator

We apply the quadratic maximum likelihood (QML) method [46, 47, 5] to the partial-sky velocity and galaxy overdensity data to reconstruct the full-sky velocity-galaxy cross-power $C_\ell^{v\alpha g\beta}$ and compare them to fiducial calculations. QML is an optimal estimator for the power spectrum of a Gaussian field with an arbitrary mask, and can extract more SNR than the common but sub-optimal pseudo- C_ℓ estimator. Our implementation of the estimator also features an analytically calculated covariance matrix, rather than one estimated from MCMC, which would require a large amount of simulated maps.

Data vector. The data vector used for QML is constructed from the pixel-space galaxy overdensity maps and the co-added kSZ reconstructed velocity maps such that $\mathbf{d}^T = (\mathbf{g}^T, \mathbf{v}^T) = (\delta_g^1, \delta_g^2, \dots, \delta_g^{10}, v^1, v^2, \dots, v^{10})$. Here each δ_g^α represents a galaxy overdensity map in redshift bin α and each v_f^α represents a velocity map reconstructed from the QE in redshift bin α . It is noted that the maps contain only the unmasked pixel in both galaxy and CMB survey. For this analysis with an overlapping sky fraction of around 22%, the number of pixels included for each map in $N_{\text{side}} = 32$ will be approximately 3000 pixels. We note that this pixel resolution should be sufficient to obtain the full SNR, because $\ell_{\text{max}} = 3N_{\text{side}} - 1 = 95$, and as we show below SNR converges at around $\ell \simeq 50$ for our data.

Optimal Quadratic Estimator. As described in [46, 47, 5], we construct the estimator for the power spectrum as follows:

$$\hat{C}_b = \mathbf{d}^T \mathbf{Q}_b \mathbf{d}, \quad (17)$$

here \hat{C}_b 's are the QML estimated powers. The indexing of b covers all the power spectrum modes constructed from the fields in the data vector. We compute the QML estimation up to $\ell_{\text{max}} = 60$ for all the power spectrum constructed from a 40-field data vector, so that b ranges from $b = 0$ to $b = 49199$. The matrix \mathbf{Q}_b is computed for each mode and is determined by the following equation:

$$\mathbf{Q}_b = \frac{1}{2} \sum_{b'} (F^{-1})_{bb'} \mathbf{C}^{-1} \mathbf{P}_{b'} \mathbf{C}^{-1}, \quad (18)$$

the matrix $\tilde{\mathbf{C}}$ is the pixel-space covariance matrix that includes both the signal computed from the fiducial power spectrum and the noise that depends on the survey properties, explicitly:

$$\begin{aligned} \mathbf{C} &= \mathbf{S} + \mathbf{N}, \\ &= \begin{pmatrix} \mathbf{C}^{gg} & \mathbf{C}^{gv} \\ \mathbf{C}^{vg} & \mathbf{C}^{vv} \end{pmatrix} + \begin{pmatrix} \mathbf{N}^{gg} & 0 \\ 0 & \mathbf{N}^{vv} \end{pmatrix}, \end{aligned} \quad (19)$$

with each term understood to be a smaller block matrix that contains all the entries from different redshift bin correlation. The noise covariance matrix \mathbf{N} is assumed to be uncorrelated between two different pixels and redshift bins. \mathbf{P}_b is the Legendre matrix in pixel space for a particular mode b and is purely geometric, which means that it depends only on the separation between two pixels from the fields in the data vector.

Fisher matrix. The Fisher matrix \mathbf{F} is also precomputed from the definition:

$$F_{bb'} = \frac{1}{2} \text{Tr}(\mathbf{P}_b \mathbf{C}^{-1} \mathbf{P}_{b'} \mathbf{C}^{-1}), \quad (20)$$

Eq. 18 implies that the QML estimator for mode b is the sum of individual contributions from all modes b' , weighted by the corresponding inverse Fisher element. The detailed definitions of \mathbf{P}_b and $(F^{-1})_{bb'}$, in Eq. 18 can be found in [46, 47, 5]. In general, each evaluation to the fisher element requires an $O(N^3)$ operation, where $N \approx 120000$ is the number of unmasked pixels multiplied by the number of fields involved. Therefore, a full calculation of the Fisher matrix can be a computationally challenging process. However, one can utilize the fact that \mathbf{P}_b is very sparse in the scenario of a large number of input fields, therefore simplifying the calculation by breaking large matrix multiplication into smaller ones [46, 5]. Additionally, one can use the addition theorem of spherical harmonics to reduce further the number of operations needed to compute the trace. We refer the readers to our upcoming companion paper on the QML estimator, which is a Python-based, optimized implementation of the QML estimator over an arbitrary number of correlated fields on partial sky. Due to our extensive optimizations, the full power spectrum analysis, including calculating the Fisher matrix, at the resolution used in this paper, takes only about one hour on a computing node. We have tested the unbiasedness of our estimator and the correctness of its covariance matrix extensively on Gaussian simulations, confirming that it outperforms the pseudo- C_ℓ as expected. These tests will be presented in an upcoming companion paper on our QML estimator.

Mode purification. The QML in its general form will use all quadratic combinations of the data for an optimal estimate, i.e. estimates of the cross-power of galaxies and velocities would contain information also from auto-powers of these fields. In the present case, auto-powers are affected by calibration issues, and we thus want to exclusively use quadratic combinations of two different fields (galaxies and velocities). This issue is similar to the traditional QML method applied to the CMB analysis, where there is an "E- to-B mode leakage" issue.

Since the goal of our analysis is to establish the signal-to-noise of the cross correlation, the variance should not include the contribution from the auto powers. Alternatively, one can set up the mode-purified covariance matrix \mathbf{C} by manually zeroing out fiducial velocity-galaxy cross-powers. such that the QML estimators \mathbf{Q}_i constructed from the new covaraiance matrix acquire zero contributions from auto-correlations, i.e. $\mathbf{v}^T \mathbf{Q}_b \mathbf{v} = \mathbf{g}^T \mathbf{Q}_b \mathbf{g} = 0$, where \mathbf{v} and \mathbf{g} are the data vectors for the galaxy and velocity maps.

The mode-purified pixel-space covariance matrix is given by:

$$\mathbf{C}_{\text{mode-purified}} = \begin{pmatrix} \mathbf{C}^{gg} + \mathbf{N}^{gg}, & 0 \\ 0 & \mathbf{C}^{vv} + \mathbf{N}^{vv} \end{pmatrix}. \quad (21)$$

This technique was already proposed in [46, 5] in the CMB context. We point out that we indeed need to set the cross-powers to zero in the covariance, even though these are the powers we want to measure. These weights ensure that only combinations of form (v, g) have non-zero weights, while (g, g) and (v, v) are nulled out. This is also consistent with the definition of the detection SNR as the significance of the rejection of the null hypothesis, because our null hypothesis is that the reconstructed velocities are not correlated with the galaxies.

Iterating the QML fiducial power. As described in [46, 5], the QML estimator is only exactly optimal if the fiducial powers in the estimator match the true data distribution (which is to be measured). It is shown in [47] that the choice of a fiducial power spectrum can affect the error bars in the signal-dominated regime, which is the case for the velocity-galaxy power spectrum at large scale. Therefore the QML estimator is sometimes used iteratively: One first estimates best fit model parameters using some fiducial covariance, and then updates the fiducial covariance with the new model parameters to run the estimator again. This will converge to optimal measurements. In our case, we found that our fiducial value for the so-called optical depth degeneracy parameter b_v is not very close to the inferred value. We therefore did a second round of QML estimation with updated parameters (we updated an overall redshift independent amplitude A , not individual bin-wise b_v , since these are noisy). Indeed, as we will see, this improves the signal-to-noise of the cross-correlation somewhat.

2.5 Fiducial Powers

As shown in Eq. 18, the construction of QML estimators relies on the fiducial power, this includes the velocity autopowers $C_\ell^{v_\alpha v_\beta}$ and the galaxy autopowers $C_\ell^{g_\alpha g_\beta}$ for any two redshift bins (α, β) selected from the ten defined in Sec. 2.1.2. Although velocity-galaxy cross-powers $C_\ell^{v_\alpha g_\beta}$ are not required for QML estimators, they are still involved in the SNR calculations of the cross-power as described in Sec. 2.6. The formulas are presented as various redshift-binned angular power spectrum C_ℓ 's in terms of their three-dimensional analogue $P(k)$'s. For the large-scale power spectra we have compared our own implementation of the integrals below with the results from `pyCCL` and found consistency. Unless otherwise specified, we use the results from `pyCCL` [11].

Galaxy power spectrum on large scales and galaxy bias. We calculate the galaxy angular power spectrum between two redshift bins (α, β) as follows:

$$C_\ell^{g^\alpha g^\beta} = \frac{2c^2}{\pi} \int dz^\alpha dz^\beta W^\alpha W^\beta \int dk k^2 P_{2h}^{g^\alpha g^\beta}(k) j_\ell(k\chi^\alpha) j_\ell(k\chi^\beta), \quad (22)$$

here c is the speed of light. W is the normalized redshift bin window function to account for the photo- z error. Their implicit dependence on the redshifts is denoted by the superscript α and β . $P^{g^\alpha g^\beta}(k)$ gives the two-halo term of the three-dimensional linear galaxy cross power between α and β . To the linear order $P^{g^\alpha g^\beta}(k)$ can be computed through the galaxy autopowers using $P^{g^\alpha g^\beta}(k) = \sqrt{P^{g^\alpha g^\alpha}(k) P^{g^\beta g^\beta}(k)}$. The integral over the wavenumber k includes the spherical Bessel functions $j_\ell(k\chi)$, where χ is the comoving distance.

The fiducial linear galaxy autopowers are calculated from matter power spectrum $P_{2h}^{m^\alpha m^\alpha}(k)$ using the following relation:

$$P_{2h}^{g^\alpha g^\alpha}(k) = (b_{g^\alpha}^2 + f\mu^2) P_{2h}^{m^\alpha m^\alpha}(k), \quad (23)$$

here $b_{g^\alpha}^2$ is the standard redshift-dependent galaxy bias, f is the redshift-space distortion parameter and $\mu = \hat{k} \cdot \hat{r}$ is the line-of-sight projection factor. The scale-dependent term $f\mu^2$ then accounts for the correction to the galaxy power spectrum due to redshift-space distortion, which is important on large scale but vanishes on small scale.

To determine the galaxy biases, the following chi-square expression

$$\chi_\alpha^2 = \sum_{\ell \in [138, 225]} \left(\tilde{C}_\ell^{g^\alpha g^\alpha} - b_{g^\alpha}^2 C_{\ell, 2h}^{m^\alpha m^\alpha} \right) \quad (24)$$

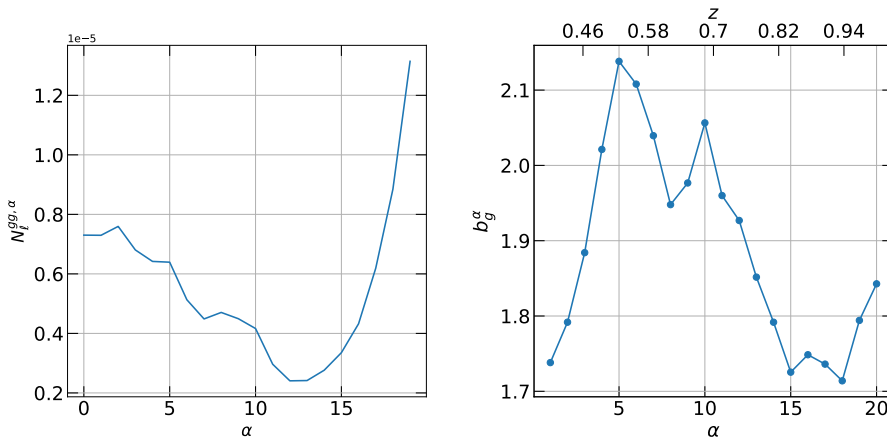


Figure 9: Left: A figure of the best-fit galaxy bias to the data across the redshift bins. The biases are defined with respect to the fiducial matter power spectrum C_ℓ^{mm} , which is computed using PyCCL [11], such that on large scale $C_\ell^{gg, \alpha} = (b_g^\alpha)^2 C_\ell^{mm}$. Right: The galaxy shot noise N_ℓ^{gg} for the 20 redshift bins α , units in steradian. They are computed from Eq. 25, with the galaxy number density obtained from the DESI LRG extended sample.

Galaxy shot noise. The QML estimator also requires a fiducial input for the noise of the galaxy autopowers $N_\ell^{gg, \alpha}$, which is there to replace the one-halo term. It can be directly translated from the galaxy number density n_{g^α} :

$$N_\ell^{gg, \alpha} = \frac{4\pi}{n_{g^\alpha}}, \quad (25)$$

which is uniform over ℓ at a given redshift bin α . In fact, at the scales where the kSZ signal is significant ($\ell > 2000$), all 20 bins are shot noise dominated. We also include a plot for the shot noise used for this analysis in the left panel of Fig. 9.

Velocity power spectrum on large scales. From the linear theory that relates the radial velocity mode and matter density modes, we write down the fiducial angular velocity autopower power and fiducial the angular cross power between velocity fields and galaxy density fields in the similar manner as Eq. 22

$$\begin{aligned} C_\ell^{\alpha v^\beta} &= \frac{2c^2}{\pi} \int dz^\alpha dz^\beta (faH)^\alpha (faH)^\beta W^\alpha W^\beta \int dk P_{2h}^{m^\alpha m^\beta}(k, z^\alpha, z^\beta) j'_\ell(k\chi^\alpha) j'_\ell(k\chi^\beta), \\ C_\ell^{v^\alpha g^\beta} &= \frac{2c^2}{\pi} b_{g^\beta} \int dz^\alpha dz^\beta (faH)^\alpha W^\alpha W^\beta \int dk k P_{2h}^{m^\alpha m^\beta}(k, z^\alpha, z^\beta) j'_\ell(k\chi^\alpha) j_\ell(k\chi^\beta). \end{aligned} \quad (26)$$

Here $f(a)$, a , and $H(a)$ are the logarithmic growth, the scale factor, and the Hubble parameter, respectively. We used the integration trick described in the Appendix of [28] to convert the extra mode dependence k into derivatives of the spherical Bessel functions for velocity fields.

Electron galaxy cross-power on small scales. As mentioned in Sec. 2.2, the kSZ quadratic estimator requires a fiducial input of the electron-galaxy cross-power $C_\ell^{\tau g, \alpha}$. Unlike $C_\ell^{v^\alpha v^\beta}$, which only requires large-scale powers, $C_\ell^{\tau g, \alpha}$ has to be calculated up to $\ell > 3000$ in order to filter the kSZ signal in the CMB maps that are of the same scale. In practice, we split the calculation of $C_\ell^{\tau g, \alpha}$ into the 1-halo term and 2-halo term, both are calculated using the Limber approximation. For the 2-halo contribution:

$$C_{\ell, 2h}^{\tau g, \alpha} = b_{g^\alpha} \sigma_T n_{e,0} \int dz^\alpha W^\alpha \left(\frac{1+z^\alpha}{\chi^\alpha} \right)^2 \int dk P_{2h}^{em, \alpha}(k, z^\alpha), \quad (27)$$

here σ_T is the Thomson cross-section, $n_{e,0}$ is the mean electron density at $z=0$, b_{g^α} is the best-fit galaxy bias such that $P_{2h}^{eg, \alpha} \approx b_{g^\alpha} P_{2h}^{em, \alpha}$ on large scale. The 2-halo electron-matter power spectrum $P_{2h}^{em, \alpha}$ is calculated using Python code `hmvec` with the Battaglia AGN-type electron profile as input [44, 2]. On small scale, the 1-halo term $C_{\ell, 1h}^{\tau g, \alpha}$ becomes important:

$$C_{\ell, 1h}^{\tau g, \alpha} = \sigma_T n_{e,0} \int dz^\alpha W^\alpha \left(\frac{1+z^\alpha}{\chi^\alpha} \right)^2 \int dk P_{1h}^{eg, \alpha}(k, z^\alpha), \quad (28)$$

we obtain $P_{1h}^{eg, \alpha}$ directly from the `hmvec` using the same electron profile. In addition, $P_{1h}^{eg, \alpha}$ requires a halo occupation model (HOD) that describes the relation between the number galaxy and the halo mass. We adopt a 5-parameter vanilla model with the best-fit LRG parameters reported by [48] for the DESI one-percent survey. The sum $C_\ell^{\tau g, \alpha} = C_{\ell, 2h}^{\tau g, \alpha} + C_{\ell, 1h}^{\tau g, \alpha}$ is used as the input for kSZ reconstruction for our main result.

We have also experimented with a simpler prescription for $C_\ell^{\tau g, \alpha}$ using a biasing model instead of an HOD:

$$C_{\ell, 1h, \text{bias}}^{\tau g, \alpha} \approx b_{g^\alpha} \sigma_T n_{e,0} \int dz^\alpha W^\alpha \left(\frac{1+z^\alpha}{\chi^\alpha} \right)^2 \int dk P_{1h}^{em, \alpha}(k, z^\alpha), \quad (29)$$

We compare the overall $C_\ell^{\tau g, \alpha}$ in the left panel of Fig. 10 and the ratio $C_{\ell, 1h, \text{bias}}^{\tau g, \alpha} / C_{\ell, 1h}^{\tau g, \alpha}$ in the right panel. In our main analysis, we use the HOD version of Eq. (28) which is more physical, not the bias model.

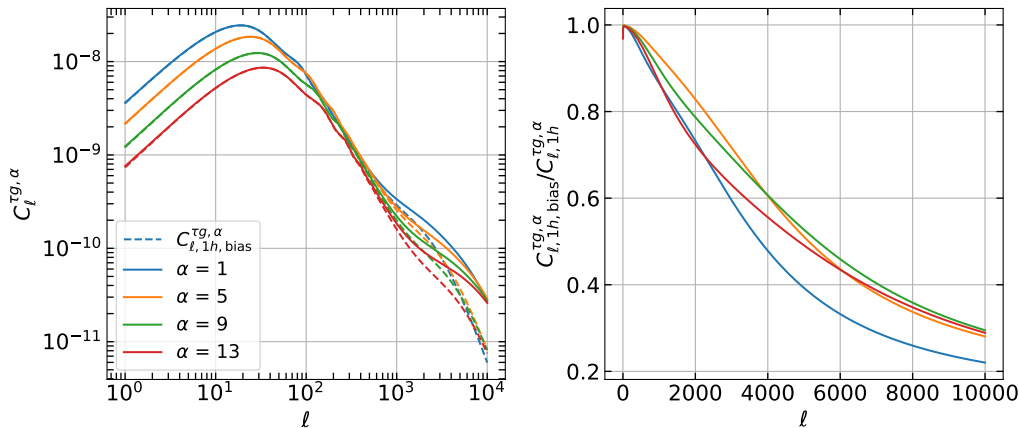


Figure 10: The electron-galaxy cross-powers $C_\ell^{\tau g, \alpha}$ for four redshift bins $\alpha = 1, 5, 9, 13$. The linear power spectrum involved in the calculation are obtained from `hmvec` using the DESI one-percent survey LRG parameters [48] for galaxy HOD and Battaglia 'AGN' model [2] for the electron profile. Left: The total electron-galaxy cross-powers $C_\ell^{\tau g, \alpha}$ from summing the one-halo and the two-halo term, dashed line shows the same curve with the one-halo term replaced by the galaxy bias approximation $C_{\ell, 1h, \text{bias}}^{\tau g, \alpha}$. Right: the ratio of the one-halo term with galaxy bias approximation (Eq. 29) to the one derived from the galaxy HOD (Eq. 28).

2.6 Cross-Correlation Signal-to-Noise

We will frame the discussion of the cross-correlation SNR in terms of the (red-shift dependent) velocity bias. The velocity bias b_v of the kSZ velocity reconstruction is the proportionality factor $v_{\text{kSZ}}(\mathbf{k}) = b_v v(\mathbf{k})$ between large-scale modes of the matter velocity field and large-scale modes of the kSZ reconstructed velocity field.

This factor would be unity if the electron distribution in halos were precisely known, i.e. for a correct P_{ge} the estimator would be unbiased by construction. The uncertainty on the electron distribution leads on large-scales to the so-called kSZ optical depth degeneracy and can be parametrized by a linear bias factor. We refer to [44] for a discussion of the optical depth degeneracy and a possible redshift dependence of b_v . Since b_v is also the amplitude of the kSZ signal ($b_v = 0$ would mean no kSZ), in each redshift bin i we will detect the kSZ individually with $\text{SNR}_\alpha = \frac{\hat{b}_v^\alpha}{\sigma_\alpha}$. Alternatively, we can fit an overall redshift independent amplitude so that $b_{v,\alpha} = A$ for all redshift bins. In this case, our overall significance is $\text{SNR} = \frac{\hat{A}}{\sigma_A}$. We now discuss these definitions in more detail.

Our goal is to establish the significance of the detection of the velocity from kSZ reconstruction, hence, we focus on the velocity-galaxy cross-powers. We define our signal as QML estimates of vg cross spectra and define the total signal-to-noise in terms of the velocity biases b_v^α in each redshift bin. We consider the following likelihood function:

$$-2\ln \mathcal{L} \left(\hat{\mathbf{C}}^{vg}, \mathbf{C}^{vg}, b_v^\alpha \right) = \left(\hat{\mathbf{C}}^{vg} - \mathbf{C}^{vg} (b_v^\alpha) \right)^T \text{Cov}^{-1} (\mathbf{C}^{vg}) \left(\hat{\mathbf{C}}^{vg} - \mathbf{C}^{vg} (b_v^\alpha) \right), \quad (30)$$

here $\hat{\mathbf{C}}^{vg}$ is understood as a vectorized output of the QML estimator that contains all independent velocity-galaxy cross powers.

It takes the following explicit form:

$$\hat{\mathbf{C}}_{vg} = \left(\hat{C}_0^{v^1 g^1}, \hat{C}_1^{v^1 g^1}, \dots, \hat{C}_{\ell_{\max}-1}^{v^{20} g^{20}}, \hat{C}_{\ell_{\max}}^{v^{20} g^{20}} \right)^T, \quad (31)$$

the vectorized power spectrum contains the velocity biases as the modeling parameters, and is expressed as:

$$\mathbf{C}_{vg} = \left(b_v^1 C_0^{v^1 g^1}, b_v^1 C_1^{v^1 g^1}, \dots, b_v^{20} C_{\ell_{\max}-1}^{v^{20} g^{20}}, b_v^{20} C_{\ell_{\max}}^{v^{20} g^{20}} \right)^T \quad (32)$$

We can introduce the matrix that assigns biases, so that

$$\mathbf{C}_{vg}(b_v^\alpha) = \mathbf{L} \mathbf{b}_v, \quad (33)$$

where \mathbf{b}_v :

$$\mathbf{b}_v = (b_v^1, b_v^2, \dots, b_v^{20})^T \quad (34)$$

is a vector of length of 20, and \mathbf{L} is as follows:

$$\mathbf{L} = \begin{pmatrix} C_0^{v^1 g^1}, & \dots, & C_{\ell_{\max}}^{v^1 g^{20}}, & 0, & \dots, & 0, & \dots, & 0 \\ 0, & \dots, & 0, & C_0^{v^2 g^1}, & \dots, & C_{\ell_{\max}}^{v^2 g^{20}}, & \dots, & 0 \\ \vdots & \vdots \\ 0, & \dots, & 0, & 0, & \dots, & 0, & \dots, & C_{\ell_{\max}}^{v^{20} g^{20}} \end{pmatrix}^T, \quad (35)$$

The optimal bias vector \mathbf{b} can then be solved analytically for the linear modeling Eq. 33. It admits the following solution:

$$\hat{\mathbf{b}}_v = (\mathbf{L}^T \text{Cov}^{-1} (\mathbf{C}^{vg}) \mathbf{L})^{-1} \left(\mathbf{L}^T \text{Cov}^{-1} (\mathbf{C}^{vg}) \hat{\mathbf{C}}^{vg} \right) \quad (36)$$

and

$$\text{Cov}^{-1}(\hat{\mathbf{b}}_v) = \mathbf{L}^T \text{Cov}^{-1} (\mathbf{C}^{vg}) \mathbf{L} \quad (37)$$

The inverse covariance matrix is just the QML Fisher matrix defined in Eq. 20, for the mode-purified case it only depends on the autopowers and the noise models:

$$\text{Cov}^{-1} (\mathbf{C}) = \mathbf{F} (\mathbf{C}^{gg}, \mathbf{C}^{vv}, \mathbf{N}^{gg}, \mathbf{N}^{vv}), \quad (38)$$

ng the power spectrum for both QML and pseudo- C_ℓ pipeline in App. D

In the case of a one-parameter amplitude fit, the estimator for the overall amplitude is

$$\hat{A} = \frac{\mathbf{b}_v^T \text{Cov}^{-1}(\hat{\mathbf{b}}_v) \hat{\mathbf{b}}_v}{\mathbf{b}_v^T \text{Cov}^{-1}(\hat{\mathbf{b}}_v) \mathbf{b}_v} \quad (39)$$

and the SNR is given by

$$\text{SNR} = \frac{\hat{A}}{\sigma_A} = \frac{\mathbf{b}_v^T \text{Cov}^{-1}(\hat{\mathbf{b}}_v) \hat{\mathbf{b}}_v}{\sqrt{\mathbf{b}_v^T \text{Cov}^{-1}(\hat{\mathbf{b}}_v) \mathbf{b}_v}}, \quad (40)$$

where here $\mathbf{b} = \mathbf{1}$ is the fiducial value. This is the definition of SNR we use as our main result. Alternatively, one could define SNR assuming no knowledge of the red shift dependence of b_v , i.e. all $b_{v,i}$ are independent variables and we exclude the null hypothesis of all $b_{v,i}$ being zero. In that case the SNR would be defined as

$$SNR = \sqrt{\hat{\mathbf{b}}_v \text{Cov}^{-1}(\hat{\mathbf{b}}) \hat{\mathbf{b}}_v} \quad (41)$$

We refer to the C for an in-depth discussion of these definitions.

The SNR in Eq. (41) is an upper limit on the SNR in Eq. (40). We note that to convert the SNR in Eq. 41 to a p-value for the detection, one would use a χ^2 distribution with the appropriate degrees of freedom. If the SNR is interpreted as sigmas of a Gaussian distribution, the appropriate definition is Eq. 40. We will use Eq. 40 as our default definition.

3 Results: kSZ Velocity Reconstruction and Cross-Correlation

We present the main results of this paper: QML estimates for the velocity-galaxy cross-powers, the estimated kSZ amplitude, and the SNR for the detection of the cross-power in this section.

3.1 kSZ velocity field reconstruction with ACT and DESI-LS

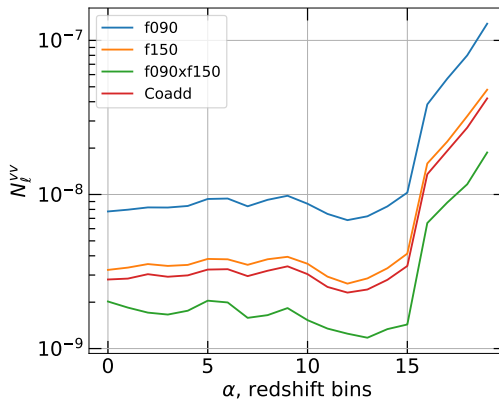


Figure 11: A summary of the kSZ reconstruction noises $N_\ell^{vv,\alpha}$ used in this analysis. The reconstruction noises are assumed to be uncorrelated between different redshift bins and nearly a constant across the multipoles ℓ . The blue and orange curves gives the noise which the velocity maps are individually reconstructed from 90 GHz and 150 GHz CMB maps. The green curve shows the cross channel kSZ noise computed from Eq. 12. The coadded noise in the red blue curve is first computed in the pixel space and converted back to harmonic space.

We applied the quadratic kSZ velocity estimator from Sec. 2.2 to the ACT and DESI-LS data described in Sec. 2.1.2. Some example sky maps are shown in Fig 18 and discussed further below.

Reconstruction noise. Fig. 11 shows the redshift dependence of various kSZ reconstruction noise $N_\ell^{vv,\alpha}$ involved in the analysis. As discussed in Sec. 2.2, we assume that the noises are uncorrelated in the pixel space and are independent of ℓ on large scales. The reconstructions noises are all calculated from the theory Eq. 11, Eq. 12 and Eq. 15. The single frequency channel noises and the cross channel noise are used as input to compute the coadded velocity maps and the associated coadded reconstruction noises.

kSZ Velocity Estimator Auto-Power Spectrum. We present the full-sky velocity autopowers $C_\ell^{vv,\alpha}$ for the 20 redshift bins recovered from the QML estimator in Fig. 12. Although the QML method provides a reconstruction for individual mode, we bin the velocity autopowers in each redshift bin in bandpowers of 6 modes using a uniform, normalized window function for the purpose of illustration. We also provide the fiducial velocity autopowers $C_\ell^{vv,\alpha}$, which is obtained by adding the fiducial signal and the rescaled reconstruction noises. The fiducial powers are convolved with the same bandpowering window function and appear to be noise dominated at $\ell > 12$ for most of the redshfit bins. Most of the data points are consistent with the fiducial powers within the 1 sigma interval and above zero. We note that the auto-powers of the kSZ reconstruction are noise dominated, except for the lowest ℓ bins, which are most contaminated by systematics. For this reason we require a cross-correlation measurement to establish a detection.

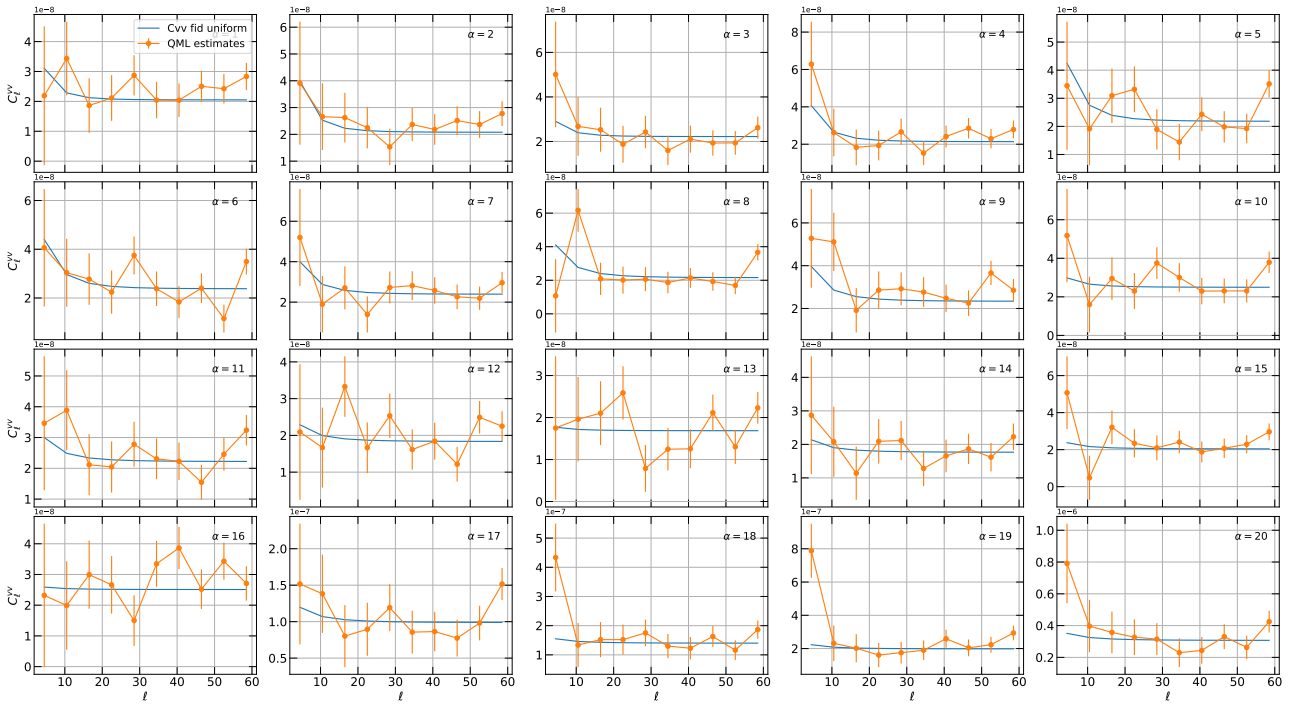


Figure 12: QML estimates of the velocity auto-powers $C_\ell^{vv, \alpha}$ computed from the kSZ reconstructed velocity maps. The data and errorbars cover modes between $\ell = 7$ to $\ell = 60$ in bandpowers of 6. The fiducial powers are plotted as the blue curves, with the kSZ reconstruction noise $N_{\ell, \text{rescaled}}^{vv, \alpha}$ included.

3.2 Velocity-Galaxy Cross-Power Spectrum

We now make the main measurement of this work, the cross-power signal-to-noise between the kSZ velocity reconstruction and the galaxy field on large scales, using our QML power spectrum estimator. A different option would be to first estimate a velocity map from the galaxy map and then cross-correlate this velocity-from-galaxy map with the velocity-from-kSZ map. However, for a linear velocity reconstruction, the resulting cross-correlation SNR would be identical to the one from a direct cross-correlation with the galaxy field in our dense matrix approach. For visualization purposes we also perform a velocity-from-galaxy reconstruction in Sec. 4, but we do not use it to establish the cross-correlation SNR. We now explain our kSZ velocity to galaxy density cross-correlation measurement.

Evaluating the covariance matrix. We first evaluate the covariance matrix analytically, which is given by the inverse of Eq. (20). The left panel in Fig. 13 shows the covariance between the cross-power $C_\ell^{g_s, v^{11}}$ and cross-powers with other redshift bin configurations (α, β) at two fixed modes $\ell = 15$ and $\ell = 20$. The x-axis iterates in an ordering of (α, β) , $(\alpha, \beta + 1)$, ..., $(\alpha, \beta + 20)$, $(\alpha + 1, \beta)$ and vice versa. One can see that the autocorrelation always gives the maximum covariance, followed by the covariance with the two nearby redshift bin configurations (7, 11) and (9, 11), which are approximately 0.8 and 0.75 of the auto covariances. This is consistent with physical intuition that the cross-power at a particular redshift bin configuration correlates with itself most, and becomes less correlated as it goes to redshift configurations that are further. It is also noted that the large covariance with nearby redshift configurations suggests the existence of significant off-diagonal components in the covariance matrix, which is expected with a fine redshift binning in this analysis.

The cross-power covariance matrix is also presented with two fixed redshift configurations $(\alpha, \beta) = (2, 1)$, $(2, 6)$ in the right panel of Fig. 13. We consider the covariances between $\ell = 20$ and modes that are centered around it. The overall profile falls as the modes move away from $\ell = 20$, suggesting an universal behavior of which the two modes become less correlated if they are further separated.

In our SNR analysis we use the full cross-power covariance matrix, such that all couplings between the modes and the redshift are properly considered. We also include two blocks of covariance matrix extracted from the full 50020×50020 version in Fig. 14, with the left plot showing the log-absolute covariance for $\ell = 20$ that is centered at $(\alpha_1, \beta_1) = (\alpha_2, \beta_2) = (8, 11)$ and the right plot centered at $(\ell_1 = \ell_2 = 30)$.

Galaxy-Velocity Cross-Power Spectrum Measurement. We then measure the cross-powers using the QML estimator in Eq. (17). The full set of galaxy-velocity cross-powers is of size 20 galaxy bins \times 20 velocity

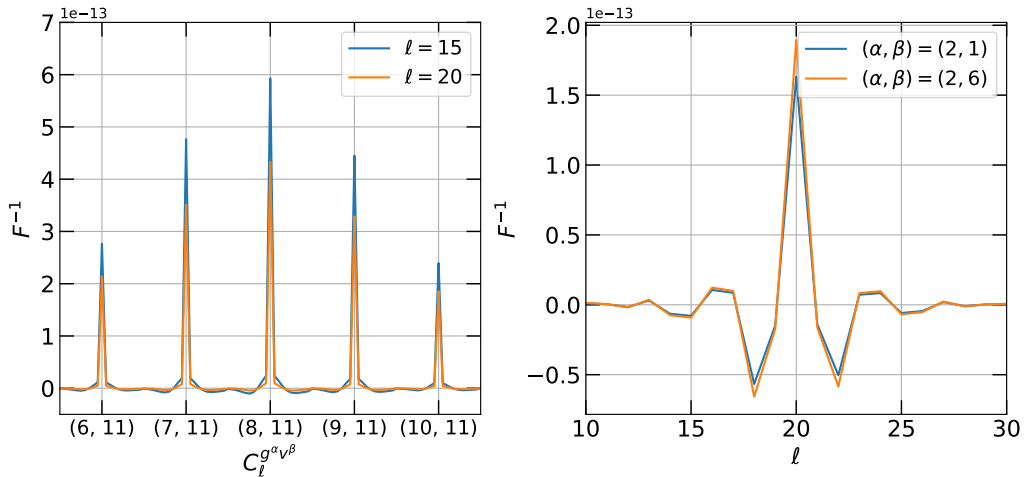


Figure 13: Left: A figure that shows the covariance of the cross-powers between the redshift bin combination $(\alpha, \beta) = (8, 11)$ and other redshift combinations centered around it for two different values of multipoles $\ell = 15$ and $\ell = 20$. The self-covariance is the largest and becomes less correlated as the redshift bins gradually move away from $\alpha, \beta = (8, 11)$. Right: Similar to the left plot but for two fixed redshift bin configurations $(\alpha, \beta) = (2, 1), (2, 6)$ and varying ℓ 's around the mode $\ell = 20$, again the covariance is the largest when coupling to itself and damps as the modes go further away from the center.

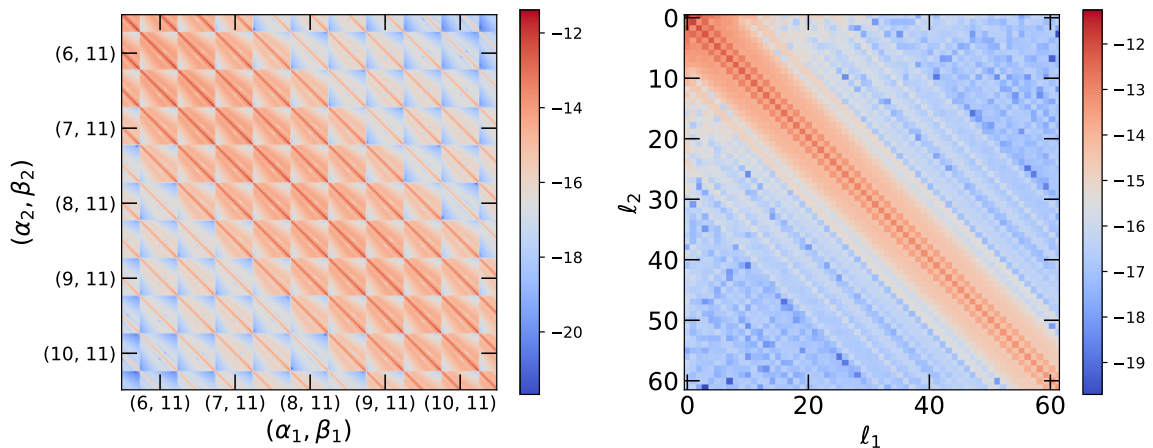


Figure 14: Left: Part of the analytic covariance matrix between the first cross power in redshift bin (α_1, β_1) and the second cross power in redshift bin (α_2, β_2) for one mode $\ell = 10$. Right: Similar to left but for $(\alpha_1, \beta_1) = (\alpha_2, \beta_2) = (2, 6)$ and varies across the modes ℓ_1, ℓ_2 .

bins = 400 cross-powers and is plotted in App. H. Here we present a set of 16 redshift-bin averaged galaxy-velocity cross-powers in Fig. 15 which are reduced from the 400 cross-powers. This is achieved by binning the redshifts in intervals of 5 and the modes in bandpowers of 6. Cross-powers have most of the correlations reside in nearby redshift bins, such that a simple bandpowering scheme across the modes is insufficient to describe the data. We outline the bandpower scheme used for Fig. 15 in App. E. Indeed, with a coarse bandpowering, one can still see that most of SNR comes from the cross-powers where the galaxy and velocity intervals are separated by 1, and are consistent with zeros as the separation between the redshift bin grows.

There are some outliers in the cross-powers at low ℓ , which are visible in the bin-averaged plots as well as in the full 20x20 cross-powers shown in App. H (which is the data we use to calculate the cross-power SNR). We find that for cross-correlation bins i, j where the theory is significantly non-zero, our data points are consistent with the model. For very off-diagonal correlations (where the expected model signal is zero), we find some outliers. For instance, the first band power in the bottom left corner of Fig. 15 is roughly 3σ away from the theory. This is likely due to remaining systematics, especially photo-z errors. However, these off-diagonal cross-correlations do not contribute significantly to our fitted amplitude and SNR (see in particular the ℓ_{min} cut experiment shown in Fig. 17 and discussion below).

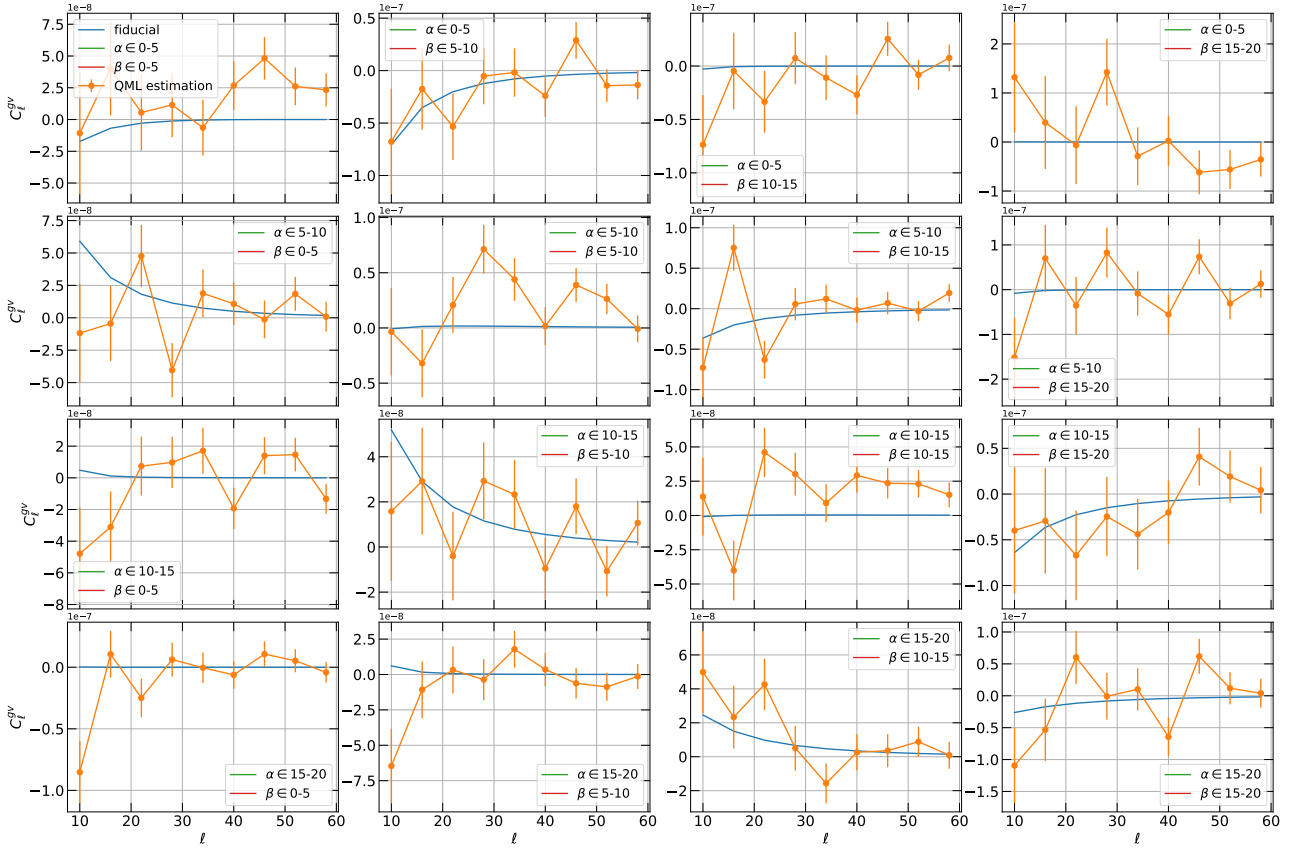


Figure 15: QML estimates of the 16 galaxy-velocity cross-powers formed by averaging from the 20×20 redshift bin configurations in redshifts of 5 and bandpowers of 6. Rescaled kSZ reconstruction noises are used for the QML estimators. Most of SNR resides in the 1st-off diagonal plots, where the galaxy redshift interval and velocity redshift interval are nearby. Data points located at cross-powers with distant redshift separations (bottom left and top right) may contain some systematics at the lowest ℓ , but contribute negligible SNR to the overall amplitude. Note that this bin-averaged plot is for illustration only, and is not used in the SNR reported in this analysis. See main text for more details and App. H for the full 400 plots used for SNR calculation.

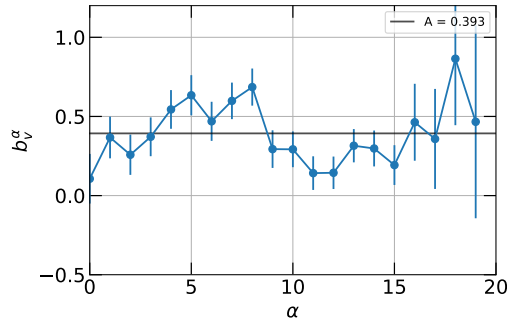


Figure 16: The best-fit velocity biases \mathbf{b}_v obtained from analytic solution Eq. 36 over the 20 redshift bins. The errorbars are retrieved from the diagonal terms of the covariance matrix for the velocity biases. The biases are defined with respect to a halo model calculation of $C_{g\tau}$ using the Battaglia profile, as explained in Sec. 2.5.

Best-fit velocity biases and overall amplitude. Fig. 16 shows the 20 velocity biases obtained from the QML velocity-galaxy cross-powers, using the linear model from Eq. 33. The velocity biases and the errorbars are solved analytically through Eq. 36 and Eq. 37. We also estimate the overall amplitude A using Eq. 40. Most of the values are consistent with the estimated overall amplitude $A = 0.39$ relative to the Battaglia model. The the last few redshift bins tend to converge to a larger b_v^α , but with large error bars. Our measurement of a relatively small A is consistent with a high feedback in massive halos (see [18]) and also consistent with the independent analysis which appears in parallel to this paper in [25].

Total Signal-To-Noise. A summary on the SNRs with different setups is shown in Table 1, where we use the range $\ell = 7$ to $\ell = 60$ to avoid the largest modes which are most strongly affected by systematics. To increase the total SNR of the cross-correlation, we run two iterations of the QML, as described at the bottom of Sec. 2.4. In the first iteration, we measure $A = 0.39 \pm 0.04$ for the kSZ amplitude. Then we adjust $C_{g\tau}$ by this value in the second iteration of the QML (i.e. we learned in the first iteration that the halo model has over-estimated the expected kSZ signal). The QML, unlike the pseudo- C_ℓ , is not invariant under this rescaling, as we explain in more detail in App. D. This procedure gains about two σ in the cross-correlation significance.

We also provide two definitions of the SNR: A 1-parameter model that represents the velocity-galaxy cross power A , which is the same across all modes and redshift bins (Eq. 40) and a 20-parameter model where each parameter represents the velocity bias of a redshift bin α (Eq. 41). We provide the SNRs for both definition in Table 1. As discussed above, if the SNR is interpreted as the significance of the rejection of the null hypothesis, the first definition as a 1-parameter model is more appropriate. In any case, the two definitions only differ by about one sigma. We thus chose the significance of the one parameter fit in the second QML iteration as our final result, giving an SNR of 11.7. We also examine the influence of the tSZ cluster mask, and find almost no change in the SNR, whether the mask is applied or not. This is in line with the findings in [30]. Finally, for an analysis with identical choices using the pseudo- C_ℓ formalism we refer to G, where we find 6.06σ cross-correlation significance and an amplitude of $A = 0.52$. The improvement with the QML is quite large, demonstrating the power of the approach.

Configuration	Amplitude A	Error σ_A	SNR (20 biases)	SNR (A/σ_A)
A_{init} (QML iteration 1)	0.393	0.0420	10.6	9.35
A_{fit} (QML iteration 2)	1.06	0.0923	12.5	11.5
A_{init} (QML iteration 1), no tSZ mask	0.382	0.0400	10.7	9.55
A_{fit} (QML iteration 2), no tSZ mask	0.979	0.0839	12.6	11.7

Table 1: Summary of the estimated velocity-galaxy cross-power amplitude, 1σ uncertainty and the signal-to-noise ratio from the first and second QML iteration, all quantities are computed from the QML estimates between $\ell = 7$ and $\ell = 60$ using a mode-by-mode Fisher matrix. Our key results are the amplitude with respect to the halo model $A = 0.39$ (QML iteration 1), and the total SNR of the cross-correlation in the second QML iteration of 11.7σ .

Dependence on ℓ_{min} We investigate the robustness of the QML estimator with respect to the choice of ℓ_{min} in Fig. 17. The left plot shows the cross power amplitude A , which falls around 0.39 at the first QML iteration and becomes close to 1 after the rescaling in the second QML iteration (by definition). The value of cross-power amplitude barely changes below $\ell = 25$, suggesting that our QML estimator gives consistent results. In the middle plot we show how the uncertainty on the amplitude scales with ℓ_{min} , showing that most signal-to-noise comes from the lower ℓ . The plot on the right gives the SNR as a function of ℓ_{min} . An interesting aspect of this plot is that the second QML iteration only improves the SNR in the regime where the analysis is strongly signal dominated. This is in line with the expectation from our analysis in App. D, where we show that in the noise dominated regime the QML becomes invariant under a rescaling of the fiducial model, in the same way as the pseudo- C_ℓ .

Optimality and future improvements. Our analysis, in terms of data representation and power spectrum estimator, should be close to optimal. In App. B we explore redshift binning and ℓ range using a Fisher forecast. This Fisher forecast uses the full pixel-wise covariance matrix, so it takes into account the survey geometry. By reducing from 20 bins to 10 bins we only find a small loss in SNR, and we again find convergence in ℓ_{max} at around 60, which is well covered with our NSIDE of 32. On the other hand, other aspects of our analysis are likely sub-optimal. For example, we do not consider anisotropic noise (even though this is technically easy to do in our dense matrix representation), and do not weight by photo- z error. We will improve these choices in future work.

4 Results: Linear Velocity Map Reconstruction from Galaxy Over-Density maps

In Sec. 3.1 we presented the results of the velocity fields that are reconstructed from the kSZ QE. Alternatively, one can utilize the linear relation between the overdensity fields and the velocity fields to reconstruct the large-scale velocity field from the density field. This method has been adopted in [33, 30] to reconstruct the 3-dimensional, linear velocity field. In addition, one can cross-correlate the velocity field from the galaxy reconstruction to the kSZ reconstruction, forming a cross-power $C^{v_{\text{gal}}v_{\text{kSZ}}}$ between the two fields. This method

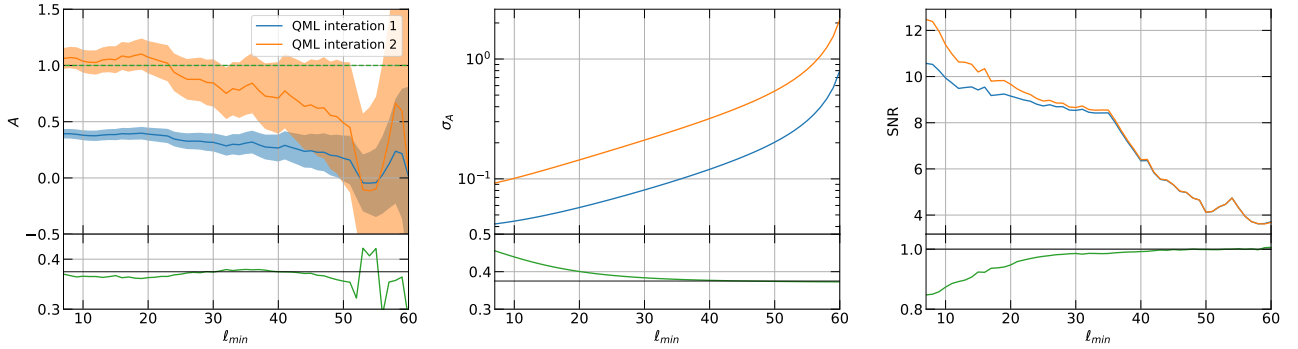


Figure 17: Summary of the QML galaxy-velocity cross-power analysis, blue and orange curve give the results in the first and second QML iteration. The quantities are plotted against different values of ℓ_{\min} , the lowest mode used for SNR calculation. Left: the velocity-galaxy cross-power amplitude A , such that $A = 1$ (green dashed line) implies a perfect agreement with the theory. The $1\text{-}\sigma$ regions are also highlighted as the shaded region. Middle: The $1\text{-}\sigma$ values computed from the fiducial power and covariance, the curves are completely analytic and are monotonically increasing with less number of modes involved in the SNR calculation. Right: The total SNR for the 20 velocity biases (Eq. (41)), note that this quantity does not equal the 1-parameter model A/σ_A . Bottom row: the ratio of the corresponding quantities in the first and second QML iteration.

allows SNR to be evaluated by comparing $C^{v_{\text{gal}}v_{\text{kSZ}}}$ to the fiducial velocity autopower. Mathematically, the SNR obtained from this method is equivalent to that obtained from cross-correlating the galaxy overdensity field with the kSZ reconstruction (Sec. 3.2), because a linear transformation does not change the SNR in the cross-correlation. However, the former provides a natural way to visualize the correlation in the map level, since both maps are velocity fields from different reconstruction method. We therefore develop a similar velocity map reconstruction method in the context of projected 2-dimensional redshift bins which aligns with the setup on the galaxy sample in this analysis.

4.1 Linear reconstruction

We formulate a pixel-space, linear estimator for the velocity map from the galaxy overdensity map as follows:

$$\hat{v}_{i,g} = M_{ij}\delta_g^j, \quad (42)$$

where the index i, j runs over all the unmasked pixels and redshift bin index α to account for the potential coupling of between pixels due to incomplete sky coverage and coupling between redshift bins. We use the subscripted variable $\hat{v}_{i,g}$ to differentiate it from the kSZ reconstruction. We look for an optimal estimator by minimizing the variance ($\langle (\hat{v}_{i,g} - v_i)(\hat{v}_{i,g} - v_i)^T \rangle$) with respect to M_{ij} , this gives:

$$\mathbf{M} = \mathbf{C}^{vg} (\mathbf{C}^{gg})^{-1}, \quad (43)$$

where $\mathbf{C}^{vg} = \langle \mathbf{v}\mathbf{g}^T \rangle$ and $\mathbf{C}^{gg} = \langle \mathbf{g}\mathbf{g}^T \rangle = \mathbf{C}_{2h}^{gg} + \mathbf{N}^{gg}$ are the fiducial pixel-space covariance matrix for the velocity-galaxy cross-power and galaxy autopower, they are identical to the components defined in Eq. 19 for the signal covariance matrix. It is noted that the estimator Eq. 43 can also be derived from maximizing the joint probability distribution between the observed galaxy overdensity maps and the underlying velocity maps that are assumed to be described by fiducial velocity power spectrum. We refer interested readers to App. F for more details.

To compare the galaxy-reconstructed velocity fields with the kSZ reconstructed ones, we compute the following correlation coefficient R_ℓ :

$$R_\ell = \frac{C_\ell^{\hat{v}_g \hat{v}}}{\sqrt{C_\ell^{\hat{v}_g \hat{v}_g} C_\ell^{\hat{v} \hat{v}}}}, \quad (44)$$

where \hat{v} refers to the velocity field from kSZ. From the mathematical form of Eq. 44 one can conclude that R_ℓ is insensitive to linear bias, such that if \hat{v}_g is identical to \hat{v} then the correlation coefficient is automatically normalized to 1. We use R_ℓ to evaluate the performance of galaxy reconstruction hereafter.

4.2 Result on DESI-LS

We apply the estimator Eq. 42 to the DESI LS LRG data described in Sec. 2.1.2 to reconstruct the velocity fields. Results for four redshift bins ($\alpha = 8, 9, 12, 17$) are presented in the left column in Fig. 18. To stress the

correlation between the velocity maps from different reconstruction method in the signal-dominated regime, we apply a filter to the modes, such that only $7 < \ell < 20$ are preserved in the maps. We compare the galaxy reconstruction to those from the kSZ reconstruction, which are given in the right column of Fig. 18. The kSZ velocity fields shown are mean-subtracted. One can find some similarities between the galaxy reconstructions and the kSZ reconstructions by eye, but given that the 11σ SNR is split over the correlation of 20 times 20 bins, no very strong visual correspondence is expected. Further, the excess in the galaxy auto-powers on large scales may lead to a bias in the galaxy-based velocity reconstruction (see Fig. 5, at $\ell < 10$). We defer a more detailed investigation of systematics in this velocity estimate to future work.

The similarities in the velocity structure between the two maps are quantified in Fig. 19 in terms of the cross-correlation coefficient. The velocity estimator \hat{v} defined for the correlation coefficient R_ℓ in Eq. 44 is now given by the kSZ reconstructions instead of the true velocity fields. The cross-correlation coefficient fluctuates within a range from -0.1 to 0.4 on large scale, showing a strong preference of a positive correlation. It is also expected that the correlation between the galaxy reconstruction and kSZ reconstruction is washed out on smaller scales, where the kSZ velocity autopowers become noise-dominated. We find that most of the redshift bins give a correlation coefficient between 0 and 0.3 with a 1-sigma significance within the signal-dominated regime $0 < \ell < 20$. We also analyze a setup by re-binning the DESI LRG catalog into 4-bins (not shown in this paper) and found a downgraded significance in the correlation coefficient, since the linear velocity estimator relies mostly on the galaxy overdensity information from nearby redshift bins, while a setup with large redshift bins tend to remove the correlation between them.

We also investigated the expected correlation coefficient between galaxy and kSZ reconstruction with Gaussian simulations. These simulation results are presented in App. F.2.

5 Conclusion

In this paper, we applied kSZ velocity reconstruction to data from ACT DR6 and DESI-LS DR9. We established the kSZ signal with a significance of 11.7σ , which is the highest SNR achieved with this method to date (equal with [25], published at the same time). We found a kSZ amplitude of $A \simeq 0.4$ with respect to the halo model prediction, again in a close match to [25], which performed their analysis independently from us. This value of A is consistent with strong feedback in massive halos, which was also found in other studies [18]. These works are also the first to establish a cross-correlation of the kSZ velocity reconstruction with a photometric galaxy field on large scales (rather than a velocity reconstruction from spectroscopic data). We also provided a linear estimator for redshift binned velocity reconstruction from a photometric galaxy over-density.

To achieve our cross-correlation measurement, we developed a novel implementation of the optimal QML power spectrum estimator, adapted to redshift-binned scalar fields. We found that this estimator substantially outperforms the traditional pseudo- C_ℓ formalism. Our estimator is somewhat unusual in that we calculate and invert the full dense covariance matrix, which is tractable at the resolution of 2×20 bins and $\ell_{max} = 60$ after some computational and algorithmic optimizations. For most analyses in cosmology, this approach would be computationally prohibitive, but for kSZ velocity reconstruction, where almost all the SNR comes from the largest scales, it is appropriate and convenient. This work is the first that demonstrates the capability of the QML pipeline to handle a large number of correlated binned fields. We will describe our QML approach and code in more detail in an upcoming companion paper.

In future work, we will extend our analysis to include cosmological parameter inference, especially of primordial non-Gaussianity f_{NL} , as proposed in [36]. Our pipeline is convenient for this purpose, as again the signal comes from the largest scales. We expect that the dense matrix approach will be convenient to include anisotropic noise or to down-weight calibration contaminated modes. f_{NL} measurements with kSZ reconstruction have already been made in [44, 30], which demonstrated the feasibility and promise of the method.

kSZ velocity reconstruction has a bright future, with SNR predicted in the hundreds for the upcoming generation of CMB and galaxy surveys [44]. The present pipeline provides a powerful starting point for future kSZ velocity reconstruction-based cosmology analysis with these experiments.

Acknowledgements

We thank Fiona McCarthy and Selim Hotinli for discussions and in particular Matthew Johnson and Kendrick Smith for comments on our draft that improved our analysis. M.M., Y.K. and A.L acknowledge the support by the U.S. Department of Energy, Office of Science, Office of High Energy Physics under Award Number DE-SC0017647, the support by the National Science Foundation (NSF) under Grant Number 2307109 and the Wisconsin Alumni Research Foundation (WARF).

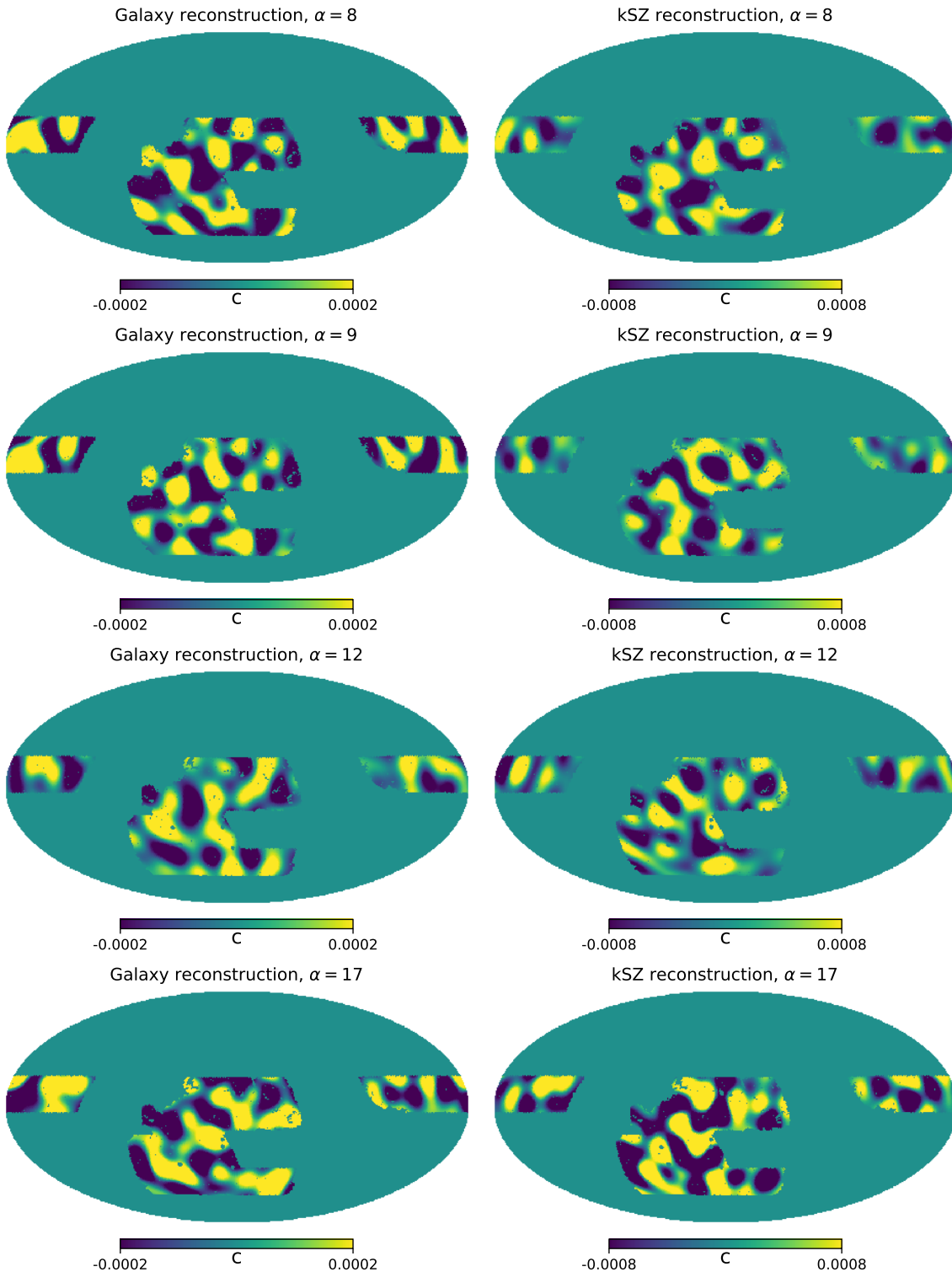


Figure 18: A side-by-side comparison between the kSZ reconstructed velocity field and the galaxy reconstructed velocity field. Modes below $\ell = 7$ and above $\ell = 20$ are removed to stress the correlation between the two fields within the range of multipoles that are signal-dominated. A cutoff on the maximum and minimum reconstructed velocities is applied to the maps, with $v \in [-2 \times 10^{-4}, 2 \times 10^{-4}]$ for the galaxy reconstruction and $v \in [-8 \times 10^{-4}, 8 \times 10^{-4}]$ for the galaxy reconstruction.

References

- [1] Stefania Amodeo et al. Atacama Cosmology Telescope: Modeling the gas thermodynamics in BOSS CMASS galaxies from kinematic and thermal Sunyaev-Zel’dovich measurements. *Phys. Rev. D*, 103(6):063514, 2021. [Erratum: *Phys.Rev.D* 107, 063514 (2023)].

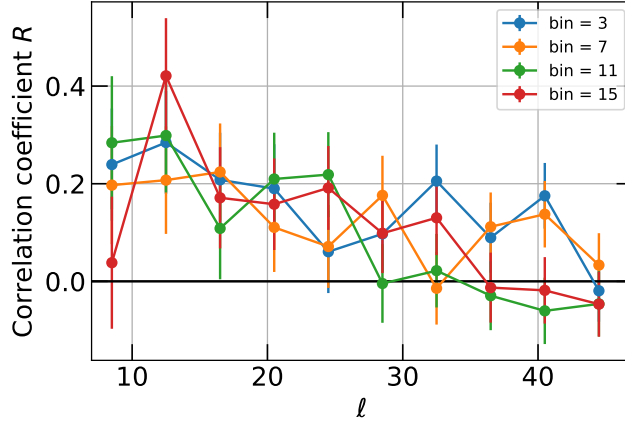


Figure 19: The correlation coefficient R_ℓ between the velocity maps from galaxy reconstruction and kSZ reconstruction for 4 redshift bins. The data point covers modes from $\ell = 7$ to $\ell = 48$ in bandpowers of 4. It can be seen that most data points lie above the black horizontal line ($R_\ell = 0$), suggesting a nonzero, positive correlation between velocity maps from the two reconstruction methods.

- [2] Nicholas Battaglia. The Tau of Galaxy Clusters. *JCAP*, 08:058, 2016.
- [3] Suman Bhattacharya and Arthur Kosowsky. Dark Energy Constraints from Galaxy Cluster Peculiar Velocities. *Phys. Rev.*, D77:083004, 2008.
- [4] Federico Bianchini and Alessandra Silvestri. Kinetic Sunyaev-Zel’dovich effect in modified gravity. *Phys. Rev.*, D93(6):064026, 2016.
- [5] J. D. Bilbao-Ahedo, R. B. Barreiro, P. Vielva, E. Martínez-González, and D. Herranz. ECLIPSE: a fast Quadratic Maximum Likelihood estimator for CMB intensity and polarization power spectra. *JCAP*, 07:034, 2021.
- [6] Richard Bloch and Matthew C. Johnson. Kinetic Sunyaev Zel’dovich velocity reconstruction from Planck and unWISE. 5 2024.
- [7] Victoria Calafut et al. The Atacama Cosmology Telescope: Detection of the pairwise kinematic Sunyaev-Zel’dovich effect with SDSS DR15 galaxies. *Phys. Rev. D*, 104(4):043502, 2021.
- [8] Juan Cayuso, Richard Bloch, Selim C. Hotinli, Matthew C. Johnson, and Fiona McCarthy. Velocity reconstruction with the cosmic microwave background and galaxy surveys. *JCAP*, 02:051, 2023.
- [9] Juan I. Cayuso and Matthew C. Johnson. Towards testing CMB anomalies using the kinetic and polarized Sunyaev-Zel’dovich effects. *Phys. Rev. D*, 101(12):123508, 2020.
- [10] Juan I. Cayuso, Matthew C. Johnson, and James B. Mertens. Simulated reconstruction of the remote dipole field using the kinetic Sunyaev Zel’dovich effect. *Phys. Rev.*, D98(6):063502, 2018.
- [11] Nora Elisa Chisari et al. Core Cosmology Library: Precision Cosmological Predictions for LSST. *Astrophys. J. Suppl.*, 242(1):2, 2019.
- [12] William Coulton et al. Atacama Cosmology Telescope: High-resolution component-separated maps across one third of the sky. *Phys. Rev. D*, 109(6):063530, 2024.
- [13] F. De Bernardis et al. Detection of the pairwise kinematic Sunyaev-Zel’dovich effect with BOSS DR11 and the Atacama Cosmology Telescope. *JCAP*, 1703(03):008, 2017.
- [14] Simon DeDeo, David N. Spergel, and Hy Trac. The kinetic sunyaev-zel’dovitch effect as a dark energy probe. 2005.
- [15] DES/SPT Collaboration et al. Detection of the kinematic Sunyaev–Zel’dovich effect with DES Year 1 and SPT. *Mon. Not. Roy. Astron. Soc.*, 461(3):3172–3193, 2016.
- [16] Anne-Sylvie Deutsch, Emanuela Dimastrogiovanni, Matthew C. Johnson, Moritz Münchmeyer, and Alexandra Terrana. Reconstruction of the remote dipole and quadrupole fields from the kinetic Sunyaev Zel’dovich and polarized Sunyaev Zel’dovich effects. *Phys. Rev. D*, 98(12):123501, 2018.

- [17] Utkarsh Giri and Kendrick M. Smith. Exploring KSZ velocity reconstruction with N-body simulations and the halo model. *JCAP*, 09:028, 2022.
- [18] B. Hadzhiyska et al. Evidence for large baryonic feedback at low and intermediate redshifts from kinematic Sunyaev-Zel’dovich observations with ACT and DESI photometric galaxies. 7 2024.
- [19] Boryana Hadzhiyska, Noah Sailer, and Simone Ferraro. Mapping the gas density with the kinematic Sunyaev-Zel’dovich and patchy screening effects: a self-consistent comparison. 6 2025.
- [20] Nick Hand et al. Evidence of Galaxy Cluster Motions with the Kinematic Sunyaev-Zel’dovich Effect. *Phys. Rev. Lett.*, 109:041101, 2012.
- [21] Carlos Hernandez-Monteagudo, Licia Verde, Raul Jimenez, and David N. Spergel. Correlation properties of the kinematic sunyaev-zel’dovich effect and implications for dark energy. *Astrophys. J.*, 643:598–615, 2006.
- [22] J. Colin Hill, Simone Ferraro, Nick Battaglia, Jia Liu, and David N. Spergel. Kinematic Sunyaev-Zel’dovich Effect with Projected Fields: A Novel Probe of the Baryon Distribution with Planck, WMAP, and WISE Data. *Phys. Rev. Lett.*, 117(5):051301, 2016.
- [23] M. Hilton et al. The Atacama Cosmology Telescope: A Catalog of >4000 Sunyaev–Zel’dovich Galaxy Clusters. *Astrophys. J. Suppl.*, 253(1):3, 2021.
- [24] Shirley Ho, Simon Dedeo, and David Spergel. Finding the Missing Baryons Using CMB as a Backlight. 2009.
- [25] Selim Hotinli, Kendrick M. Smith, and Simone Ferraro. Velocity Reconstruction from KSZ: Measuring f_{NL} with ACT and DESILS. *to appear on arxiv jointly with this paper*.
- [26] Selim C. Hotinli, James B. Mertens, Matthew C. Johnson, and Marc Kamionkowski. Probing correlated compensated isocurvature perturbations using scale-dependent galaxy bias. *Phys. Rev. D*, 100(10):103528, 2019.
- [27] Jordan Krywonos, Selim C. Hotinli, and Matthew C. Johnson. Constraints on cosmology beyond Λ CDM with kinetic Sunyaev Zel’dovich velocity reconstruction. 8 2024.
- [28] Yurii Kvasiuk, Jordan Krywonos, Matthew C Johnson, and Moritz Münchmeyer. Reconstruction of continuous cosmological fields from discrete tracers with graph neural networks. *arXiv preprint arXiv:2411.02496*, 2024.
- [29] Yurii Kvasiuk and Moritz Münchmeyer. Autodifferentiable likelihood pipeline for the cross-correlation of CMB and large-scale structure due to the kinetic Sunyaev-Zeldovich effect. *Phys. Rev. D*, 109(8):083515, 2024.
- [30] Alex Laguë, Mathew S. Madhavacheril, Kendrick M. Smith, Simone Ferraro, and Emmanuel Schaun. Constraints on local primordial non-Gaussianity with 3d Velocity Reconstruction from the Kinetic Sunyaev-Zeldovich Effect. 11 2024.
- [31] Antony Lewis and Anthony Challinor. Weak gravitational lensing of the CMB. *Phys. Rept.*, 429:1–65, 2006.
- [32] Niall MacCrann et al. The Atacama Cosmology Telescope: reionization kSZ trispectrum methodology and limits. *Mon. Not. Roy. Astron. Soc.*, 532(4):4247–4260, 2024.
- [33] Fiona McCarthy et al. The Atacama Cosmology Telescope: Large-scale velocity reconstruction with the kinematic Sunyaev–Zel’dovich effect and DESI LRGs. 10 2024.
- [34] Eva-Maria Mueller, Francesco de Bernardis, Rachel Bean, and Michael D. Niemack. Constraints on gravity and dark energy from the pairwise kinematic Sunyaev-Zeldovich effect. *Astrophys. J.*, 808(1):47, 2015.
- [35] Eva-Maria Mueller, Francesco de Bernardis, Rachel Bean, and Michael D. Niemack. Constraints on massive neutrinos from the pairwise kinematic Sunyaev-Zel’dovich effect. *Phys. Rev.*, D92(6):063501, 2015.
- [36] Moritz Münchmeyer, Mathew S. Madhavacheril, Simone Ferraro, Matthew C. Johnson, and Kendrick M. Smith. Constraining local non-Gaussianities with kinetic Sunyaev-Zel’dovich tomography. *Phys. Rev. D*, 100(8):083508, 2019.

- [37] Sigurd Naess et al. The Atacama Cosmology Telescope: arcminute-resolution maps of 18 000 square degrees of the microwave sky from ACT 2008–2018 data combined with Planck. *JCAP*, 12:046, 2020.
- [38] Sigurd Naess et al. The Atacama Cosmology Telescope: DR6 Maps. 3 2025.
- [39] Zhen Pan and Matthew C. Johnson. Forecasted constraints on modified gravity from Sunyaev-Zel’dovich tomography. *Phys. Rev. D*, 100(8):083522, 2019.
- [40] Planck Collaboration et al. Planck intermediate results. XXXVII. Evidence of unbound gas from the kinetic Sunyaev-Zeldovich effect. *Astron. Astrophys.*, 586:A140, 2016.
- [41] Mehdi Rezaie et al. Local primordial non-Gaussianity from the large-scale clustering of photometric DESI luminous red galaxies. *Mon. Not. Roy. Astron. Soc.*, 532(2):1902–1928, 2024.
- [42] Emmanuel Schaan et al. Evidence for the kinematic Sunyaev-Zel’dovich effect with the Atacama Cosmology Telescope and velocity reconstruction from the Baryon Oscillation Spectroscopic Survey. *Phys. Rev.*, D93(8):082002, 2016.
- [43] Emmanuel Schaan et al. Atacama Cosmology Telescope: Combined kinematic and thermal Sunyaev-Zel’dovich measurements from BOSS CMASS and LOWZ halos. *Phys. Rev. D*, 103(6):063513, 2021.
- [44] Kendrick M. Smith, Mathew S. Madhavacheril, Moritz Münchmeyer, Simone Ferraro, Utkarsh Giri, and Matthew C. Johnson. KSZ tomography and the bispectrum. 10 2018.
- [45] R. A. Sunyaev and Y. B. Zeldovich. The velocity of clusters of galaxies relative to the microwave background. The possibility of its measurement. *Monthly Notices of the Royal Astronomical Society*, 190(3):413–420, mar 1980.
- [46] Max Tegmark and Angelica de Oliveira-Costa. How to measure CMB polarization power spectra without losing information. *Phys. Rev. D*, 64:063001, 2001.
- [47] S. Vanneste, S. Henrot-Versillé, T. Louis, and M. Tristram. Quadratic estimator for CMB cross-correlation. *Phys. Rev. D*, 98(10):103526, 2018.
- [48] Sihan Yuan et al. The DESI one-per-cent survey: exploring the halo occupation distribution of luminous red galaxies and quasi-stellar objects with AbacusSummit. *Mon. Not. Roy. Astron. Soc.*, 530(1):947–965, 2024.
- [49] Rongpu Zhou et al. DESI luminous red galaxy samples for cross-correlations. *JCAP*, 11:097, 2023.
- [50] Rongpu Zhou et al. Target Selection and Validation of DESI Luminous Red Galaxies. *Astron. J.*, 165(2):58, 2023.

A Imaging Calibration for the DESI LRG Extended Sample

As described in Sec. 2.1.2, the DESI extended LRG example suffers an excess in the galaxy autopowers on large scale. This can partly be removed by modeling the imaging properties of the objects at different redshift bins using the observed data. We provide the 11 imaging properties + intercept and their corresponding best-fit modeling parameter in Fig. 20, note that the parameters depend on the redshift bin, such that one has to recompute the regression model and generate a new set of coefficients for each redshift bin.

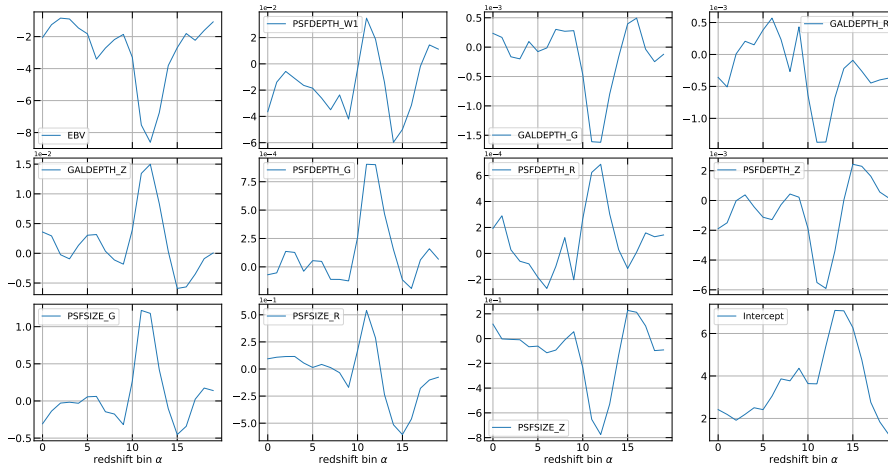


Figure 20: The imaging properties used for constructing the linear regression model and their best-fit values, the imaging maps associated to these properties are available from the data product in [50] the unit of the modeling parameters are 1/(imaging property units). The 'Intercept' panel models a constant term in addition to the 11 imaging properties in order account for potential constant bias from the data.

Fig. 21 illustrates the difference in the galaxy overdensity map before and after the imaging calibration using the second redshift bin as an example. The original random map (top right) only accounts for the biasing in galaxy counts due to the survey footprint, it is therefore inadequate to describe the actual survey condition due to lack of imaging properties. The calibrated random map, however, includes the effect from imaging systematics that can account for photometry at a particular redshift bin. For example, one can see that the calibrated random map tends to overcount the number of galaxies around zero declination. The effect of using a calibrated random map for overdensity computation is shown in the bottom row, where anomalies such as unphysical, overdense regions vanish from the overdensity maps.

B Fisher Forecast for the QML Estimator

It is known that the QML estimator is optimal for Gaussian fields. i.e., it saturates the Cramer-Rao lower bound, and therefore has the smallest possible error bars for the power spectrum. In this section, we make this statement more explicit for our application to velocity-galaxy cross-power by showing that the Fisher information obtained from the QML estimator is equivalent to the one directly obtained from the pixel space covariance matrix. We then use the Fisher matrix to study whether our redshift binning and ℓ_{max} exhaust the available SNR, using the full pixel-wise covariance matrix rather than the typical but imprecise f_{sky} approximation.

Starting from the definition of the fiducial pixel covariance matrix, $\mathbf{C}(A)$:

$$\mathbf{C}(A) = \begin{pmatrix} \mathbf{C}^{gg} + \mathbf{N}^{gg}, & A\mathbf{C}^{gv} \\ A\mathbf{C}^{vg}, & \mathbf{C}^{vv} + \mathbf{N}^{vv} \end{pmatrix}, \quad (45)$$

here we consider a redshift-independent parameter A . It is reminded that the cross-power amplitude A is included as the only parameter to be constrained in this problem. Also note that $A = 0$ recovers the mode-purified pixel space covariance matrix Eq. 19. The fisher information with respect to A is given by, according to the definition:

$$F_{AA} = \frac{1}{2} \text{Tr} \left(\mathbf{C}^{-1} \frac{\partial \mathbf{C}}{\partial A} \mathbf{C}^{-1} \frac{\partial \mathbf{C}}{\partial A} \right) \Big|_{A=0}, \quad (46)$$

as we measure the number of sigmas away from $A = 0$. Now we can write $\frac{\partial \mathbf{C}}{\partial A}$ in terms of Legendre matrix \mathbf{P}_ℓ , such that:

$$\frac{\partial \mathbf{C}}{\partial A} = \sum_{\ell \in \mathbf{C}^{vg}} C_\ell^{vg} \mathbf{P}_\ell, \quad (47)$$

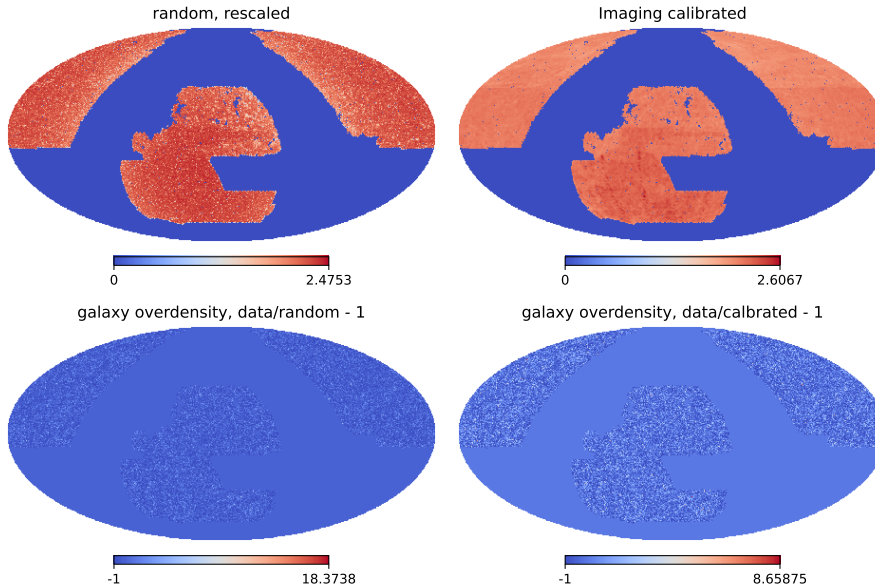


Figure 21: The imaging properties used for constructing the linear regression model and their best-fit values, the imaging maps associated to these properties are available from the data product in [49]. The last row gives the constant term in additional to the 10 imaging properties in order account for potential constant bias from the data.

rewriting the fisher information with this definition gives:

$$\begin{aligned}
 F_{AA} &= \sum_{\ell'\ell} \frac{1}{2} \text{Tr} (\mathbf{C}^{-1} C_{\ell}^{vg} \mathbf{P}_{\ell} \mathbf{C}^{-1} C_{\ell'}^{vg} \mathbf{P}_{\ell'}) \Big|_{A=0} , \\
 &= \sum_{\ell'\ell} C_{\ell}^{vg} C_{\ell'}^{vg} \frac{1}{2} \text{Tr} (\mathbf{C}^{-1} \mathbf{P}_{\ell} \mathbf{C}^{-1} \mathbf{P}_{\ell'}) \Big|_{A=0} , \\
 &= \sum_{\ell'\ell} C_{\ell}^{vg} C_{\ell'}^{vg} \mathbf{F}_{\ell\ell'}^{\text{QML}} , \\
 &= \mathbf{C}^{vg} \mathbf{F}^{\text{QML}} \mathbf{C}^{vg} ,
 \end{aligned} \tag{48}$$

$$\tag{49}$$

where from second to third row we use the definition of the QML fisher matrix Eq. 20 and we label it with a superscript 'QML' to distinguish it from the Fisher information of the cross power amplitude. We have also replaced the summation over the cross-power modes ℓ, ℓ' with a matrix multiplication of the vectorized cross-powers \mathbf{C}^{vg} . Note that the last line is equivalent to the definition of the error in cross-power amplitude σ_A using a mode-purified covariance matrix, Eq. 57. This completes the proof.

We present the fisher forecast for different covariance matrix setups in Fig. 22. The x-axis shows the number of multipoles preserved in the fisher forecast. It can be seen that the SNR starts to saturate at $\ell = 40$ for all configurations. This implies that the QML estimator can be formulated up to $\ell = 40$ without any significant loss in extra SNR. The setup with 20 bins and with the error σ_A estimated at $A = 1$ has the highest SNR among the 3 curves presented, it is three times larger than the mode-purified configuration (blue curve).

From Fig. 22 it is also clear that for a given estimated cross-power amplitude, most of the SNR are located in the first 20 modes. For the case of 20 redshift bins with mode purification (blue curve), the SNR increases by 3 in the first 10 modes and 1.5 in the next 10 modes, accounting for 75% of the total SNR. Therefore, the SNR is mainly affected by the quality of the low ℓ cross-powers reconstructed from the data.

C Definition of the SNR as a Significance of the Rejection of the Null Hypothesis

Let us define broadly the hypothesis $H_1 : \{S \neq 0\}$ that we detect some "signal", which is defined precisely later. The null hypothesis is $H_0 : \{S = 0\}$. We define SNR in all cases as

$$SNR = \sqrt{-2\Delta \ln \mathcal{L} \Big|_{H_0}} \tag{50}$$

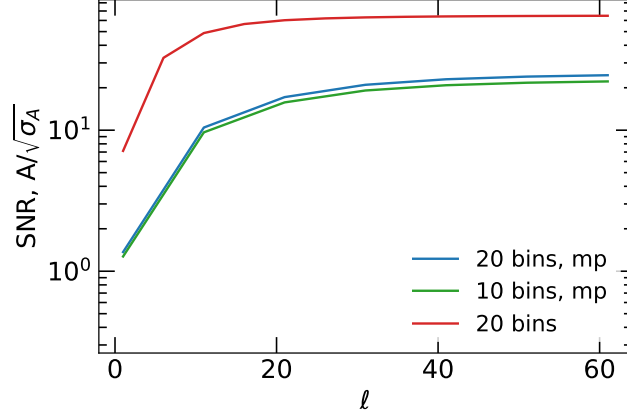


Figure 22: A figure that illustrates the fisher forecast for various configurations, the covariance matrix is computed using the prescribed fiducial powers in Sec. 2.5. 'mp' stands for a mode-purified covariance matrix. Red curve shows the SNR computed from σ_A at $A = 1$. All SNR calculations assume a C^{gv} amplitude parameter $A = 1$.

It has a nice meaning of the significance in "number of sigmas" of the rejection of H_0 . We immediately note that in the simplest possible case of one Gaussian variable, this definition implies the usual $SNR = \frac{\hat{\mu}}{\sigma}$. Let us define $\hat{\mathbf{x}}$ - an output of the QML pipeline for cross powers. Then by construction

$$-2 \ln \mathcal{L}(\mathbf{x}|\hat{\mathbf{x}}) = (\hat{\mathbf{x}} - \mathbf{x}) \mathbf{F} \Big|_{\mathbf{x}} (\hat{\mathbf{x}} - \mathbf{x}) \quad (51)$$

And hence for the null hypothesis that $\hat{\mathbf{x}}$ is consistent with noise (that is equivalent to $\mathbf{x} = \mathbf{0}$) we get

$$SNR = \sqrt{\hat{\mathbf{x}} \mathbf{F} \hat{\mathbf{x}}} \quad (52)$$

Because not all the parameters are independent parameters of our theory model, we usually define the reduced set of parameters that we are interested in: eg. \mathbf{b} : $\dim \mathbf{b} = N_b, \dim \mathbf{x} = N$, and $N_b \ll N$. Let's also define a grouping matrix \mathbf{G} , $\dim \mathbf{G} = (N, N_b)$ and diagonal matrix \mathbf{X} , $\dim \mathbf{X} = (N, N)$ with \mathbf{x} on the diagonal. Grouping matrix is a general way to group estimates with the same property. For example, one can group all the multipoles in the same pair of redshifts and define a bias coefficient for the corresponding template. Then we have

$$-2 \ln \mathcal{L}(\mathbf{b}|\hat{\mathbf{x}}) = (\hat{\mathbf{x}}^T - \mathbf{b}^T \mathbf{G}^T \mathbf{X}) \mathbf{F} \Big|_{\mathbf{x}} (\mathbf{X} \mathbf{G} \mathbf{b} - \hat{\mathbf{x}}) \quad (53)$$

This likelihood is maximized with

$$\hat{\mathbf{b}}^T = (\mathbf{G}^T \mathbf{X} \mathbf{F} \mathbf{X} \mathbf{G})^{-1} \mathbf{G}^T \mathbf{X}^T \mathbf{F} \hat{\mathbf{x}} \quad (54)$$

Then

$$-2 \ln \mathcal{L}(\mathbf{b}|\hat{\mathbf{b}}) = (\hat{\mathbf{b}}^T - \mathbf{b}^T) \mathbf{C}_b^{-1} (\mathbf{b} - \hat{\mathbf{b}}) \quad (55)$$

With $\mathbf{C}_b = (\mathbf{G}^T \mathbf{X} \mathbf{F} \mathbf{X} \mathbf{G})^{-1}$ It follows that SNR in this case is (under $H_0 : \mathbf{b} = \mathbf{0}$)

$$SNR = \sqrt{\hat{\mathbf{b}} \mathbf{C}_b^{-1} \hat{\mathbf{b}}} \quad (56)$$

We also note that in the extreme case of one parameter $\mathbf{b} = A$, we have

$$\hat{A} = \frac{\mathbf{x}^T \mathbf{F} \hat{\mathbf{x}}}{\mathbf{x}^T \mathbf{F} \mathbf{x}}, \quad \sigma_a^2 = \frac{1}{\mathbf{x}^T \mathbf{F} \mathbf{x}}, \quad SNR_A = \sqrt{\hat{A} \sigma_A^{-2} \hat{A}} = \frac{\mathbf{x}^T \mathbf{F} \hat{\mathbf{x}}}{\sqrt{\mathbf{x}^T \mathbf{F} \mathbf{x}}} \quad (57)$$

Dependent on how we define signal S : \mathbf{x} , \mathbf{b} , or A , we can use either of the expressions as a consistent definition of SNR. We adopted the definition of the SNR via \mathbf{b} in the main text, where we group according to redshift binning, so that \mathbf{b} represents the amplitude of the cross spectrum in a given bin. The SNR in Eq. (41) is an upper limit on the SNR in Eq. (40): since covariance and its inverse are positive definite, the first definition of the SNR is just a norm with respect to the inner product $(\cdot, \cdot)_{cov^{-1}}$. The inequality that relates two definitions of the SNR follows from the Cauchy-Schwarz inequality tells us that $(\hat{\mathbf{b}}, \mathbf{b})_{cov^{-1}} \leq \sqrt{(\hat{\mathbf{b}}, \hat{\mathbf{b}})_{cov^{-1}} (\mathbf{b}, \mathbf{b})_{cov^{-1}}}$. We also note that even though $SNR_A \leq SNR_{\mathbf{b}_v}$, the detection significance should be interpreted via p-value. For the case of a single variable A , $SNR_A^2 = \hat{A} \sigma_A^{-2} \hat{A} \sim \chi_1^2(SNR_A^2)$ and $p_A = 1 - F_{\chi_1^2}(SNR_A^2)$, while for \mathbf{b}_v , $p_{\mathbf{b}_v} = 1 - F_{\chi_n^2}(SNR_{\mathbf{b}_v}^2)$. Here, $F_{\chi_n^2}$ is the cumulative density function (CDF) of the χ^2 distribution with n degrees of freedom.

Comment on the alternative definition of the SNR Having estimated $\hat{\mathbf{b}}_v$, one could've defined the SNR as

$$\text{SNR} = \frac{\hat{\mathbf{b}}_v^T \text{Cov}^{-1}(\hat{\mathbf{b}}_v) \mathbf{b}_v}{\sqrt{\mathbf{b}_v^T \text{Cov}^{-1}(\hat{\mathbf{b}}_v) \mathbf{b}_v}}, \quad (58)$$

where $\mathbf{b}_v = \mathbf{1}$ as a fiducial value. Looking more carefully at this expression and recalling that $\text{Cov}(\hat{\mathbf{b}}_v)^{-1} = \mathbf{L}^T \mathbf{F} \mathbf{L}$, we can notice that it's the same as the expression of the SNR for the single amplitude. First, we note that $\mathbf{L} = \mathbf{X} \mathbf{G}$. Then

$$\mathbf{G}^T \mathbf{X} \mathbf{F} \mathbf{X} \mathbf{G} \mathbf{1} = \mathbf{G}^T \mathbf{X} \mathbf{F} \mathbf{x} \quad (59)$$

Since $\mathbf{G}^T \mathbf{X} \mathbf{F} \mathbf{X} \mathbf{G}$ is invertible, we can write

$$\mathbf{1} = (\mathbf{G}^T \mathbf{X} \mathbf{F} \mathbf{X} \mathbf{G})^{-1} \mathbf{G}^T \mathbf{X} \mathbf{F} \mathbf{x} \quad (60)$$

Then under the root we have:

$$\mathbf{x}^T \mathbf{F} \mathbf{L} (\mathbf{L}^T \mathbf{F} \mathbf{L})^{-1} \mathbf{L}^T \mathbf{F} \mathbf{x} = \text{Tr}[\mathbf{F} \mathbf{L} (\mathbf{L}^T \mathbf{F} \mathbf{L})^{-1} \mathbf{L}^T \mathbf{F} \mathbf{x} \mathbf{x}^T] \quad (61)$$

Then we notice that $\mathbf{x} \mathbf{x}^T = \mathbf{X} \mathbf{1} \mathbf{1}^T \mathbf{X}$, use cyclic identity of trace and the fact that

$$\text{Tr}[\mathbf{G}^T \mathbf{A} \mathbf{G}] = \text{Tr} \mathbf{A} \quad (62)$$

because of the property of the grouping matrix. We simplify

$$\text{Tr}[\mathbf{F} \mathbf{L} (\mathbf{L}^T \mathbf{F} \mathbf{L})^{-1} \mathbf{L}^T \mathbf{F} \mathbf{x} \mathbf{x}^T] \quad (63)$$

$$= \text{Tr}[\mathbf{G}^T \mathbf{X} \mathbf{F} \mathbf{L} (\mathbf{L}^T \mathbf{F} \mathbf{L})^{-1} \mathbf{L}^T \mathbf{F} \mathbf{X} \mathbf{G} \mathbf{1} \mathbf{1}^T] \quad (64)$$

$$= \mathbf{x}^T \mathbf{F} \mathbf{x} \quad (65)$$

Nominator can be similarly simplified, so that indeed

$$\text{SNR} = \frac{\hat{\mathbf{b}}_v^T \text{Cov}^{-1}(\hat{\mathbf{b}}_v) \mathbf{b}_v}{\sqrt{\mathbf{b}_v^T \text{Cov}^{-1}(\hat{\mathbf{b}}_v) \mathbf{b}_v}} = \frac{\mathbf{x}^T \mathbf{F} \hat{\mathbf{x}}}{\sqrt{\mathbf{x}^T \mathbf{F} \mathbf{x}}} \quad (66)$$

D Rescaling of the kSZ Estimator under Fiducial Power $C_{g\tau}$

To understand the effect to the SNR from either the QML and pseudo- C_ℓ due to potential mismodeling, we consider the case of the overall galaxy-velocity cross-power amplitude A . Consider a rescaling of fiducial $C_\ell^{\tau g}$ by a factor of b due to a mismodelling, such that $\bar{C}^{\tau g} = b C^{\tau g}$, now we ask the question how does the kSZ estimator change with it, assuming b is not scale dependent, i.e., it is not a function of ℓ , then according to the definition Eq. 7:

$$\begin{aligned} \bar{N}_\ell^{vv, \alpha} &= b^{-2} \bar{N}_\ell^{vv, \alpha}, \\ \bar{\hat{v}}_{\ell m} &= b^{-1} \hat{v}_{\ell m}, \end{aligned} \quad (67)$$

then one can ask how will the SNR for velocity-galaxy cross-power,

$$\begin{aligned} \frac{A}{\sigma_A} &= \frac{(\hat{\mathbf{C}}^{vg})^T \text{Cov}^{-1} \mathbf{C}^{vg}}{\sqrt{(\mathbf{C}^{vg})^T \text{Cov}^{-1} \mathbf{C}^{vg}}}, \\ &= \frac{(\hat{\mathbf{C}}^{vg})^T \mathbf{F} \mathbf{C}^{vg}}{\sqrt{(\mathbf{C}^{vg})^T \mathbf{F} \mathbf{C}^{vg}}}. \end{aligned} \quad (68)$$

changes with respect to the scaling, both for pseudo- C_ℓ and QML .

For pseudo- C_ℓ , since the mask decoupling is a linear operation and it does not depend on the choice of fiducial powers, one can safely propagate this scaling to the reconstructed fullsky velocity autopowers and cross-powers:

$$\begin{aligned} \bar{C}_{\ell, \text{pcl}}^{\hat{v}\hat{v}} &= b^{-2} C_{\ell, \text{pcl}}^{\hat{v}\hat{v}}, \\ \bar{C}_{\ell, \text{pcl}}^{g\hat{v}} &= b^{-1} C_{\ell, \text{pcl}}^{g\hat{v}}, \\ \bar{C}_\ell^{gv} &= C_\ell^{gv} \end{aligned} \quad (69)$$

It is noted that the fiducial powers does not scale with the mismodelling factor, since the cross-power does not contain the reconstruction noise. Moreover, the covariance of the cross-powers, which is evaluated from rescaled pcl power spectrum, is also corrected by a factor of b^{-2} :

$$\text{Cov}^{-1} = b^2 \text{Cov}^{-1}, \quad (70)$$

Then the SNR of the rescaled velocity field, Eq. 68 is given by:

$$\begin{aligned} \left(\frac{A}{\sigma_A} \right)_{\text{pcl}} &= \frac{(b^{-1})(b^2) A}{\sqrt{(b^2)} \sigma_A}, \\ &= \frac{A}{\sigma_A}, \end{aligned} \quad (71)$$

i.e. the significance of the cross-correlation estimated with pseudo- C_ℓ does not change under such a rescaling.

One the other hand, consider the QML estimator, Eq. 67-Eq. 69 still holds (since QML is unbiased over the power spectrum by constructions). However, the inverse covariance matrix/Fisher matrix are now computed from fiducial powers, we instead have the following relations:

$$\begin{aligned} \bar{F} &= \bar{F} (S_\ell^{vv} + \bar{N}_\ell^{vv}), \\ &= \bar{F} (S_\ell^{vv} + b^{-2} N_\ell^{vv}), \end{aligned} \quad (72)$$

the Fisher matrix for QML estimator depends on the fiducial velocity autopower C_ℓ^{vv} , which contains the signal S_ℓ^{vv} that does not scale with the mismodeling, and the reconstruction noise \bar{N}_ℓ^{vv} that is obtained from Eq. 67. Therefore, the QML inverse covariance matrix do not follow a simple rescaling relation as in pseudo- C_ℓ , and we arrive at the expression for the new SNR:

$$\begin{aligned} \left(\frac{A}{\sigma_A} \right)_{\text{QML}} &= b^{-1} \frac{(\hat{\mathbf{C}}^{vg})^T \bar{F} \mathbf{C}^{vg}}{\sqrt{(\mathbf{C}^{vg})^T \bar{F} \mathbf{C}^{vg}}}, \\ &= b^{-1} M(b) \frac{(\hat{\mathbf{C}}^{vg})^T F \mathbf{C}^{vg}}{\sqrt{(\mathbf{C}^{vg})^T F \mathbf{C}^{vg}}}, \\ &= b^{-1} M(b) \frac{A}{\sigma_A}, \end{aligned} \quad (73)$$

where we have defined the the function:

$$M(b) = \sqrt{\frac{(\mathbf{C}^{vg})^T F \mathbf{C}^{vg} (\hat{\mathbf{C}}^{vg})^T \bar{F} \mathbf{C}^{vg}}{(\mathbf{C}^{vg})^T \bar{F} \mathbf{C}^{vg} (\hat{\mathbf{C}}^{vg})^T F \mathbf{C}^{vg}}}, \quad (74)$$

note that $M \rightarrow 1$ as $b \rightarrow 1$. To illustrate the effect of the correction factor $b^{-1}M$ we restrict ourselves to one redshift bin and one mode, such that both C^{vg} and F are numbers. In this limit, F can be easily determined from the Gaussian covariance:

$$\begin{aligned} F^{-1} &= C^{vv} C^{gg}, \\ &= (S^{vv} + N^{vv})(S^{gg} + N^{gg}), \end{aligned} \quad (75)$$

we have omitted the subscript ℓ for simplicity and $C^{vg} = C^{gv} = 0$ for a mode-purified estimator. Apparently, $\bar{F}^{-1} \neq b^2 F^{-1}$, and the correction factor is given by:

$$\begin{aligned} b^{-1}M &= b^{-1} \sqrt{\frac{S^{vv} + N^{vv}}{S^{vv} + b^{-2}N^{vv}}}, \\ &= b^{-1} \sqrt{\frac{R^{vv} + 1}{R^{vv} + b^{-2}}}. \end{aligned} \quad (76)$$

The kSZ signal-to-noise ratio R^{vv} is defined as the ratio between the fiducial velocity autopower and kSZ reconstruction noise S^{vv}/N^{vv} . We display the function Eq. 76 in Fig. 23 for different values of mismodelling factor b and kSZ SNR R^{vv} . From the left panel one can see that in signal-dominated regime $R^{vv} > 1$, any mismodelling in the electron-galaxy power spectrum ($b \neq 1$) will induce a correction factor the cross-power SNR. In particular, $b < 1$ gives a boost in SNR, while $b > 1$ gives a drop in SNR. The correction factor converges to 1 as the kSZ reconstruction enters the noise-dominated regime $R^{vv} < 1$. To summarize, the galaxy-electron cross-power SNR obtained from the QML pipeline can vary with fiducial power spectrum input for the Fisher matrix calculation. In the regime where C_ℓ^{vg} is overestimated and the kSZ reconstruction is signal-dominated, one can record a boost in the SNR through a linear correction factor b .

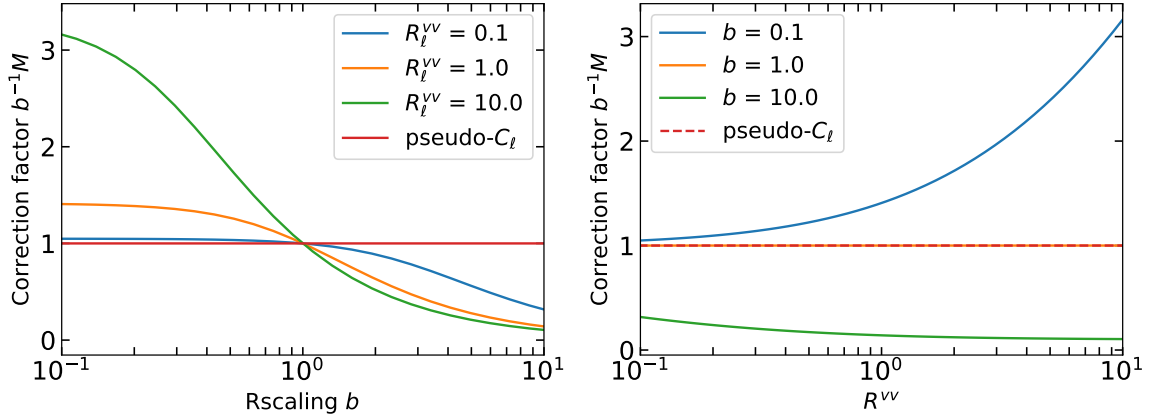


Figure 23: Illustrations of the QML SNR correction factor Eq. 76 with varying rescaling b and velocity autopower SNR R^{vv} . Left: varying b for three different values of $R^{vv} = 0.1, 1$ and 10 , corresponding to the noise-dominated, signal-noise-comparable and signal-dominated regimes. Right: varying R^{vv} for three different values of $b = 0.1, 1$ and 10 , corresponding to the underestimating, exact-modelling and overestimating of the observed velocity map. The correction factor $b^{-1}M = 1$ for pseudo- C_ℓ is also plotted as the red line (dash line for the right plot to avoid overlapping with the $b = 1$ in QML) for reference.

E Bandpowering Scheme for Velocity-Galaxy Cross-Powers

Here we briefly mention the bandpowering scheme used for making the plots in Fig. 15, which takes into account the non-zero coupling between different modes and redshift bins. Consider a bandpowered cross-power defined as follows:

$$\mathbf{C}_{(i,j,L)}^{gv} = \mathbf{M}_{(i,j,L),(\alpha,\beta,\ell)} \mathbf{C}_{(\alpha,\beta,\ell)}^{gv}, \quad (77)$$

$$= \frac{1}{V} \sum_{\substack{\alpha \in i, \\ \beta \in j, \ell \in L}} C_\ell^{g^\alpha v^\beta}, \quad (78)$$

here $\mathbf{C}_{(i,j,L)}^{gv}$ gives the bandpowered, vectorized cross-power with a new set of indexing (i, j, L) that represents the first redshift interval, second redshift interval and the bandpower. For simplicity we weight each mode equally, such that V is the normalization factor that gives the total number of modes within the interval (i, j, L) and \mathbf{M} is a rectangular matrix of dimension $(i \times j \times L)$ by $(\alpha \times \beta \times \ell)$, such that:

$$\mathbf{M}_{(i,j,L),(\alpha,\beta,\ell)} = \frac{1}{V} \text{ if } (\alpha, \beta, \ell) \in (i, j, L). \quad (79)$$

The bandpowered covariance matrix, with the diagonal terms as the squared errorbars, is compressed as:

$$\mathbf{F}_{\text{bandpowered}}^{-1} = \mathbf{M} \mathbf{F}^{-1} \mathbf{M}^T, \quad (80)$$

we note that this choice of uniform weighting across the modes is suboptimal, i.e, it leads to a loss in SNR compared to the un-binned cross-powers. This is also different from a direct 4 galaxy redshift bins \times 4 velocity redshift bin QML analysis. The purpose of Eq. 77 is to provide a simple averaging, so that qualitative features of the QML cross-powers can still be illustrated given that the complicated mixing between redshift bins and modes is minimally preserved.

F Linear Estimator of the Velocity Field from Galaxies

F.1 Construction of the Velocity Estimator from Maximizing the Joint Probability $\mathcal{P}(v_r^{\text{true}}, \delta_g^{\text{obs}})$

The true, mode-dependent radial velocity field at different slices of redshift shells $v_r^{\alpha, \text{true}}$ are correlated to each other. This is because matters in nearby region should interact with each other and move in similar velocities. We wish to reconstruct the large-scale radial velocity field from galaxy survey through linear theory. Therefore, to the lowest order, we assume the true radial velocity field can be related to observed matter tracer overdensity

δ_g , which will be the galaxy overdensity in this case. To start with, we construct the pixel-space radial velocity vector $\mathbf{v}_r^{\text{true}}$ and the galaxy overdensity vector \mathbf{g}^{true} , defined as:

$$\begin{aligned}\mathbf{v}_r^{\text{true}} &= (v_r^{\alpha_1, \text{true}}, v_r^{\alpha_2, \text{true}}, \dots, v_r^{\alpha_n, \text{true}})^{\text{T}} \\ \mathbf{g}^{\text{obs}} &= (g^{\alpha_1, \text{obs}}, g^{\alpha_2, \text{obs}}, \dots, g^{\alpha_n, \text{obs}})^{\text{T}},\end{aligned}\quad (81)$$

here α runs across a total number of redshift bins n . Each $v_r^{\alpha_n, \text{true}}$ and $g^{\alpha_1, \text{obs}}$ should be understood as the vectorized velocity and galaxy overdensity map. The radial velocity vector denotes the underlying true radial velocity distribution and the galaxy overdensity vector is based on the observed data, which is the Websky simulation in this case.

Armed with the definitions, we assume that $\mathbf{v}_r^{\text{true}}$ can be constructed from a linear model of \mathbf{g}^{obs} . That is:

$$\mathbf{v}_r^{\text{true}} = \mathbf{M} \mathbf{g}^{\text{obs}}. \quad (82)$$

The fact that Eq. 82 lies in the pixel space makes it more adaptive to the partial-sky scenario, since masking over a certain region on the sky will only reduce the dimension of the data vector and matrix \mathbf{M} in Eq. 82, while one has to account for the mode coupling between all the modes (ℓ, m) in the spherical harmonic space, such that the dimension of the matrix cannot be reduced. From the expression Eq. 82, we construct a Gaussian likelihood joint probability distribution $\mathcal{P}(\mathbf{v}_r^{\text{true}}, \mathbf{g}^{\text{obs}})$.

$$\mathcal{P}(\mathbf{v}_r^{\text{true}}, \mathbf{g}^{\text{obs}}) = \exp\left(-\frac{1}{2} \mathbf{u}^{\text{T}} \mathbf{C}^{-1} \mathbf{u}\right), \quad (83)$$

where \mathbf{u} is an abstract notation of the composite vector $\mathbf{u} = (\mathbf{v}_r^{\text{true}}, \mathbf{g}^{\text{obs}})^{\text{T}}$ and \mathbf{C} is a large covariant matrix defined as:

$$\mathbf{C} = \begin{pmatrix} C^{v_r v_r} & C^{v_r g} \\ C^{v_r g} & C^{g g} \end{pmatrix}, \quad (84)$$

each entry in the Eq. 84 represents a $n \times n$ block covariant matrix, for example:

$$C^{v_r v_r} = \begin{pmatrix} C^{v_r^1 v_r^1} & \dots & C^{v_r^1 v_r^{\alpha_n}} \\ \dots & \dots & \dots \\ C^{v_r^{\alpha_n} v_r^1} & \dots & C^{v_r^{\alpha_n} v_r^{\alpha_n}} \end{pmatrix}, \quad (85)$$

This covariant matrix is completely determined by the linear theory and can be directly calculated from the equations in last section. Assuming that $(C^{v_r v_r})^{-1}$ and $(C^{g g})^{-1}$ exist, then \mathbf{C}^{-1} can be represented as follows:

$$\mathbf{C}^{-1} = \begin{pmatrix} \mathbf{Q}(C^{v_r v_r}, C^{g g}) & -\mathbf{Q}(C^{v_r v_r}, C^{g g}) C^{v_r g} (C^{g g})^{-1} \\ -\mathbf{Q}(C^{g g}, C^{v_r v_r}) C^{v_r g} (C^{v_r v_r})^{-1} & \mathbf{Q}(C^{g g}, C^{v_r v_r}) \end{pmatrix}, \quad (86)$$

where the matrix $\mathbf{Q}(C^{v_r v_r}, C^{g g})$ is given as follows:

$$\mathbf{Q}(C^{v_r v_r}, C^{g g}) = \left(C^{v_r v_r} - C^{v_r g} (C^{g g})^{-1} C^{v_r g}\right)^{-1}, \quad (87)$$

notice that we repeatedly used the symmetric property $C^{v_r g} = (C^{g v_r})^{\text{T}}$.

Inserting Eq. 86 and the definition of \mathbf{u} to the joint probability $\mathcal{P}(\mathbf{v}_r^{\text{true}}, \mathbf{g}^{\text{obs}})$, we arrive the following expression for the exponential term:

$$\begin{aligned}\mathbf{u}^{\text{T}} \mathbf{C}^{-1} \mathbf{u} &= \left((\mathbf{v}_r^{\text{true}})^{\text{T}} \quad (\mathbf{g}^{\text{obs}})^{\text{T}} \right) \begin{pmatrix} \mathbf{Q}(C^{v_r v_r}, C^{g g}) & -\mathbf{Q}(C^{v_r v_r}, C^{g g}) C^{v_r g} (C^{g g})^{-1} \\ -\mathbf{Q}(C^{g g}, C^{v_r v_r}) C^{v_r g} (C^{v_r v_r})^{-1} & \mathbf{Q}(C^{g g}, C^{v_r v_r}) \end{pmatrix} \begin{pmatrix} \mathbf{v}_r^{\text{true}} \\ \mathbf{g}^{\text{obs}} \end{pmatrix} \\ &= (\mathbf{v}_r^{\text{true}})^{\text{T}} \mathbf{Q}(C^{v_r v_r}, C^{g g}) \mathbf{v}_r^{\text{true}} + (\mathbf{v}_r^{\text{true}})^{\text{T}} \left[-\mathbf{Q}(C^{v_r v_r}, C^{g g}) C^{v_r g} (C^{g g})^{-1} \right] \mathbf{g}^{\text{obs}} + \dots, \end{aligned}\quad (88)$$

other terms are abbreviated since they will not be involved in the minimization. Recall that we want to obtain a maximum likelihood estimation of the underlying radial velocity field $\mathbf{v}_r^{\text{true}}$. This can be achieved by minimizing the expression Eq. 88 with respect to $(\mathbf{v}_r^{\text{true}})^{\text{T}}$. All abbreviated terms vanish upon the derivative with respect to $(\mathbf{v}_r^{\text{true}})^{\text{T}}$, leaving:

$$\frac{\partial (\mathbf{u}^{\text{T}} \mathbf{C}^{-1} \mathbf{u})}{\partial (\mathbf{v}_r^{\text{true}})^{\text{T}}} = \mathbf{Q}(C^{v_r v_r}, C^{g g}) \left[\mathbf{v}_r^{\text{true}} - C^{v_r g} (C^{g g})^{-1} \mathbf{g}^{\text{obs}} \right], \quad (89)$$

setting this to zero and we immediately obtain a reconstruction of the radial velocity field:

$$\mathbf{v}_r^{\text{true}} = C^{v_r g} (C^{g g})^{-1} \mathbf{g}^{\text{obs}}, \quad (90)$$

this result is also expected from finding \mathbf{M} through the minimization of the variance

$$\left\langle (\hat{\mathbf{v}} - \mathbf{v}_r^{\text{true}}) (\hat{\mathbf{v}} - \mathbf{v}_r^{\text{true}})^{\text{T}} \right\rangle. \quad (91)$$

F.2 Validating the Velocity Reconstruction on Simulations

To explore the validity of the linear estimator Eq. 42, we construct the pixel covariance matrices \mathbf{C}^{gg} , \mathbf{C}^{vg} and \mathbf{C}^{vv} according to prescription in Sec. 2.4. We include the galaxy shot noise for the galaxy autopowers, such that $\mathbf{C}^{gg} = \mathbf{S}^{gg} + \mathbf{N}^{gg}$ while keeping only the signal for the velocity covariance $\mathbf{C}^{vv} = \mathbf{S}^{vv}$. The pixel covariance matrix spans the unmasked footprint of the DESI-LS survey on $N_{\text{side}} = 16$, accounting for a sky fraction $\approx 44\%$. We simulate full-sky, Gaussian velocity maps and galaxy maps from the same power spectrum that are used to generate the pixel covariance matrices above. Suvery mask is then applied to maps to reproduce the observation, such that the velocity fields are reconstructed from the mask galaxy overdensity maps following Eq. 42.

We provide a side-by-side comparison between the galaxy reconstruction and the underlying velocity fields directly simulated from the fiducial velocity power spectrum in Fig. 24. The reconstruction quality is high, as one can see most of structures between the scale $\ell = 7$ and $\ell = 20$ is recovered. This is partly due to the large sky coverage of the DESI-LS footprint. In general, the level of galaxy shot noise in each redshift bin increases with the number of redshift bins over a fixed interval. However, more redshift bins also implies more tomographic structure, which is important for reconstruction methods that heavily relies on the information from nearby redshifts.

The quality of the reconstruction is described more quantitatively in the left panel of Fig. 25 in terms of the correlation coefficient R_ℓ . For redshift bins that are away from the two edges of the interval ($\alpha = 3$, $\alpha = 18$), R_ℓ ranges from 0.85 to 0.95, suggesting a strong correlation between the galaxy-reconstructed velocity fields and the true velocity field. However, the correlation coefficient R_ℓ begins to fall for redshift bins that are closer to the edge of the interval ($\alpha = 1$, $\alpha = 20$). These redshift bins suffer more from not getting information beyond the interval than those away from the edge. This is because the velocity-galaxy cross-power peaks when the velocity field and galaxy fields come from nearby but not exactly the same redshift bins. In general, there is a slight drop in correlation as ℓ increases, but the effect is not obvious. To conclude, the linear estimator proposed in Sec. F is an effective way to reconstruct 2D velocity fields from 2D galaxy overdensity fields as long as the correlations between different redshift bins are properly included in the construction of the covariance matrix. The fact that the estimator is performed on pixel space also suggests that it is highly compatible with sky masks in arbitrary shapes.

G A Comparison with Pseudo- C_ℓ

To evaluate the improvement factor from adopting the QML pipeline, we perform a SNR analysis on the velocity-galaxy cross-power amplitude A using the pseudo- C_ℓ estimates, which is available from the `PyMaster` package. The input velocity maps correspond to the tsz-masked $N_{\text{side}} = 32$. Both the input velocity maps and the galaxy overdensity maps are apodized on a scale of 1 degree using the 'Smooth' scheme. We create bandpowers for every 6 modes from $\ell = 7$ to $\ell = 60$. We note that, because pseudo- C_ℓ requires apodization, it is possible that increasing N_{side} would be more beneficial to the pseudo- C_ℓ than the QML, and somewhat reduce the improvement.

To construct the covariance matrix for the pseudo- C_ℓ estimates, we generate 10^5 fullsky, Gaussian simulations using the fiducial power spectrum $C_\ell^{v^\alpha v^\beta}$, $C_\ell^{g^\alpha g^\beta}$ and $C_\ell^{g^\alpha v^\beta}$ as outlined in Sec. 2.5. Maps from each simulation are then overlaid with the overlapping mask and processed with PyMaster pipeline to obtain the pseudo- C_ℓ power spectrum. The covariance is computed from the pseudo- C_ℓ power spectrum. We present the covariance between the second bandpower of $C^{v^3 g^{11}}$ and the second bandpower of nearby redshift bins in Fig. 26. As a comparison, we also plot the covariance matrix obtained from 5×10^4 simulations. It can be observed that the covariance converges for both sets of simulations when the redshift-bin configurations (α, β) are highly correlated. However, we find that convergence is difficult to achieve for less correlated redshift bins. As a result, the SNR for the velocity-galaxy cross-power amplitude could differ by more than 1 sigma between the analysis with 5×10^4 and with 10^5 simulations. We include a summary from the pseudo- C_ℓ pipeline using the covariance matrix estimated from 10^5 simulations in Fig. 27. The velocity-galaxy cross-power amplitude A is estimated to be 0.523, with a 1-sigma uncertainty at $\sigma_A = 0.0867$, resulting in a SNR of 6.06.

H All Estimated 20×20 Bin Galaxy-Velocity Cross-Power Spectra

$$C_\ell^{gv}$$

We provide a complete set of galaxy-velocity cross-power C_ℓ^{gv} without any averaging over redshift bins in the Fig. 28-31. Each plot contains a $10 \times 10 = 100$ cross-powers that corresponds to a block from the full 20×20 plot. It is noted that while there is no averaging over redshift bins, a bandpowering from $\ell = 7$ to $\ell = 60$ in intervals of 6 is still implemented to facilitate visualization, such that the correlations between different modes may not

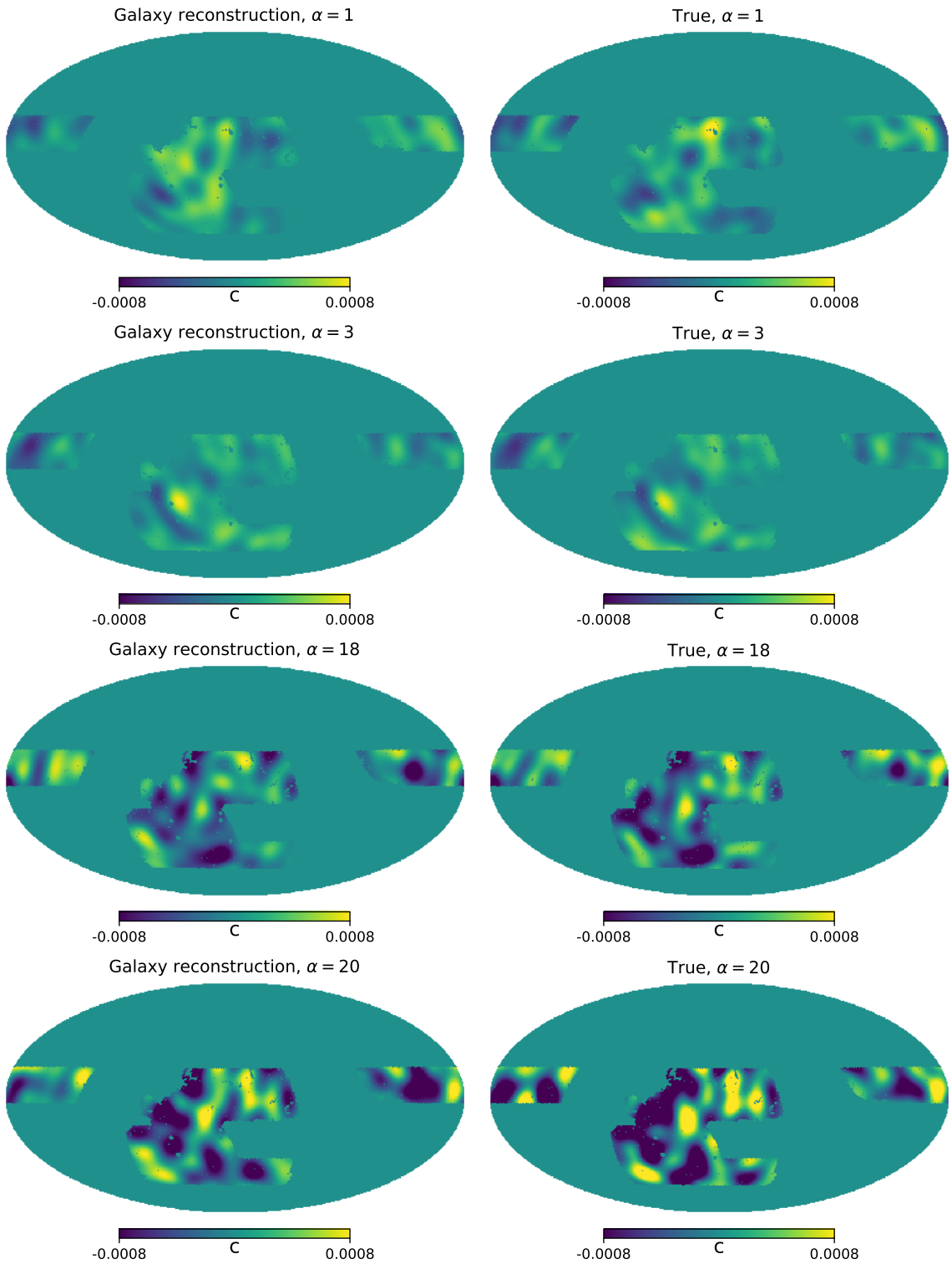


Figure 24: The velocity fields reconstructed from the masked galaxy overdensity maps (left column) to the true velocity fields (right column). The first and last two redshift bins ($\alpha = 1, 2, 19, 20$) are selected for illustration. The maps are first obtained on $N_{\text{side}} = 16$ and the projected to $N_{\text{side}} = 128$, modes with $\ell < 7$ and $\ell > 20$ are removed for better visualization.

be accurately presented. However, the SNR calculation in Sec. 3.2 uses the mode-by-mode covariance matrix, so that there is no ambiguity in the SNR values reported in Table 1.

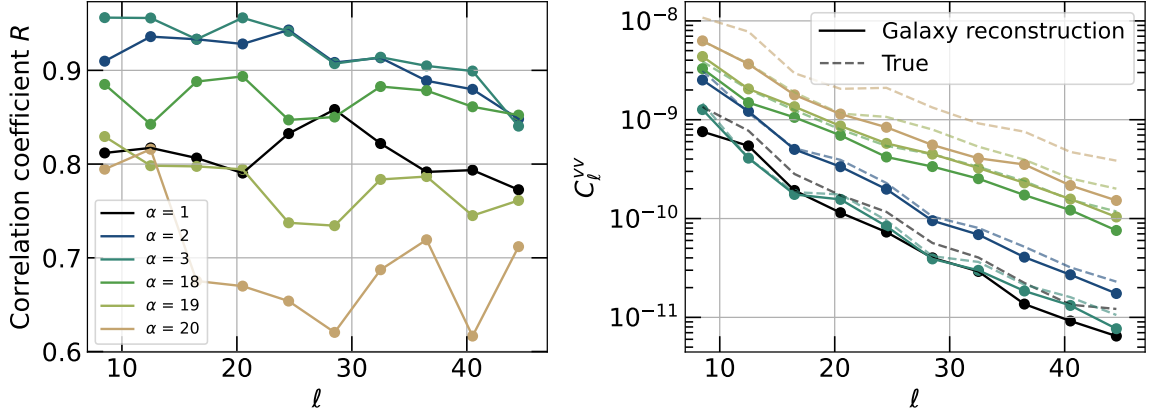


Figure 25: Left: The correlation coefficient R_ℓ between the reconstructed velocity fields and true velocity fields for redshift bins around the edge of the interval. Right: The velocity autopowers directly computed from the unmasked pixels, neither f_{sky} approximation or pseudo- C_ℓ was applied since the coupling between masks and modes are the same for both the reconstructed field and the fiducial field. A bandpowering between $\ell = 7$ to $\ell = 48$ is applied to both plots in 4 modes per bandpower.

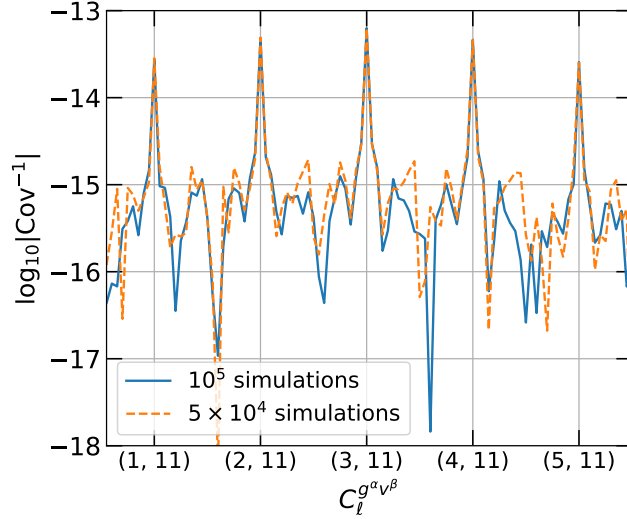


Figure 26: The covariance of the velocity-galaxy cross-power between $\alpha = 3$, $\beta = 11$ and other redshift bins for the second bandpower ($\ell \in [13, 18]$). Log-absolute is take for the covariances for the purpose of illustration. The solid line is estimated from 10^5 simulations, the dashed line is estimated from 5×10^4 simulations. Highly-correlated redshift bins with large covariances is converging for both setups, while less-correlated redshift bins with smaller covariances (1-2 orders of magnitude lower) remains numerically unstable. The numerical uncertainties can aggregate to cause a change of 0.5 to 1 sigma in the cross-power SNR.

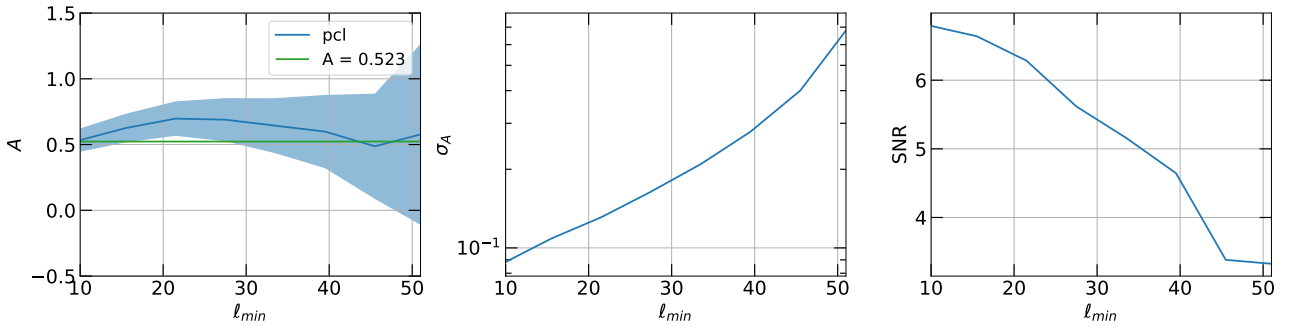


Figure 27: A summary of the results from the pseudo- C_ℓ pipeline using the covariance matrix evaluated from 10^5 simulations. The definitions of the velocity-galaxy cross-power amplitude A and 1-sigma uncertainty follows from Eq. 40. The quantities are plotted against the lower cutoff of the bandpowers.

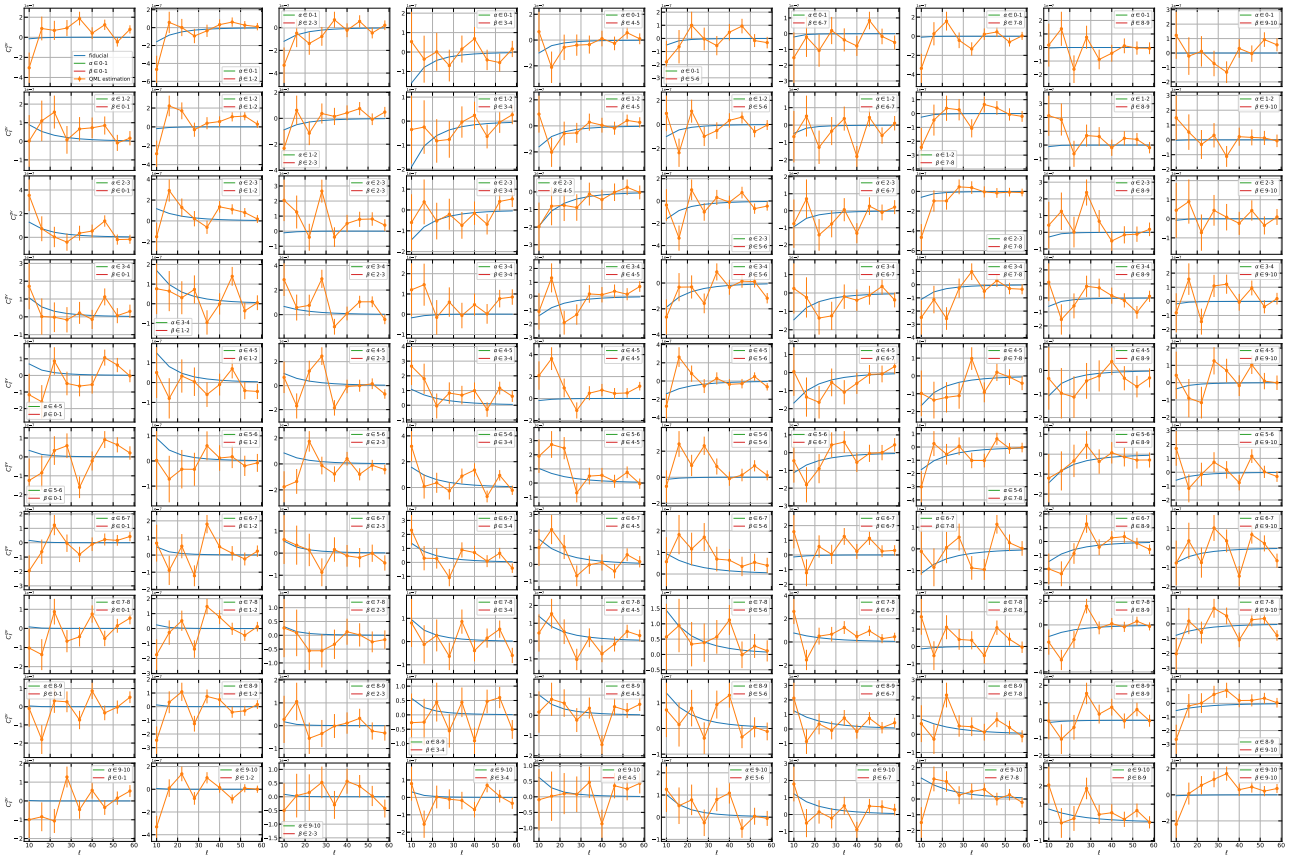


Figure 28: Part for the full 20-bins galaxy maps by 20-bins velocity maps cross-power from QML estimates. The modes are bandpowered in intervals of 6 using a uniform window function. Displaying is the $\alpha \in 1 - 10$, $\beta \in 1 - 10$ block.

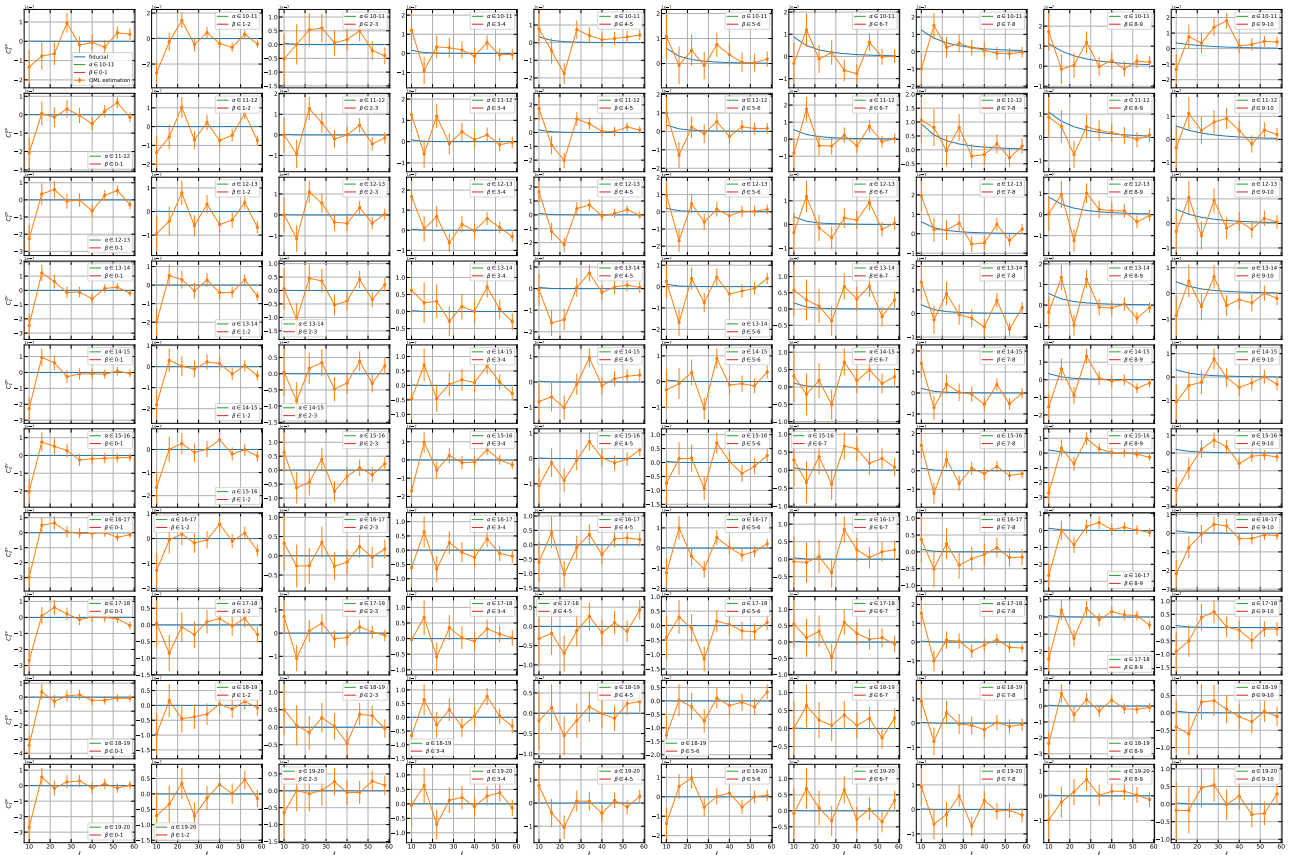


Figure 29: Same as Fig. 28 but with $\alpha \in 10 - 20$, $\beta \in 0 - 10$ block.

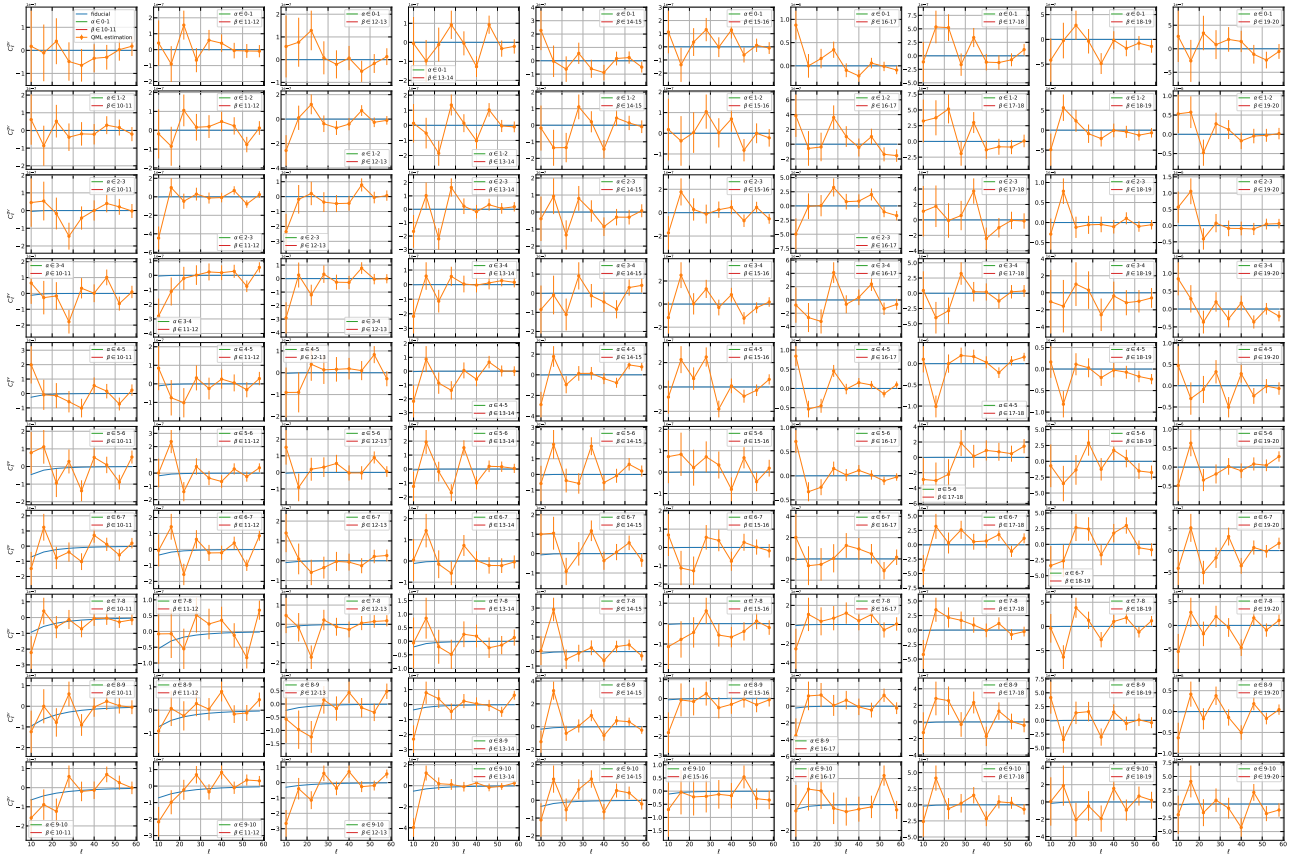


Figure 30: Same as Fig. 28 but with $\alpha \in 0 - 10, \beta \in 10 - 20$ block.

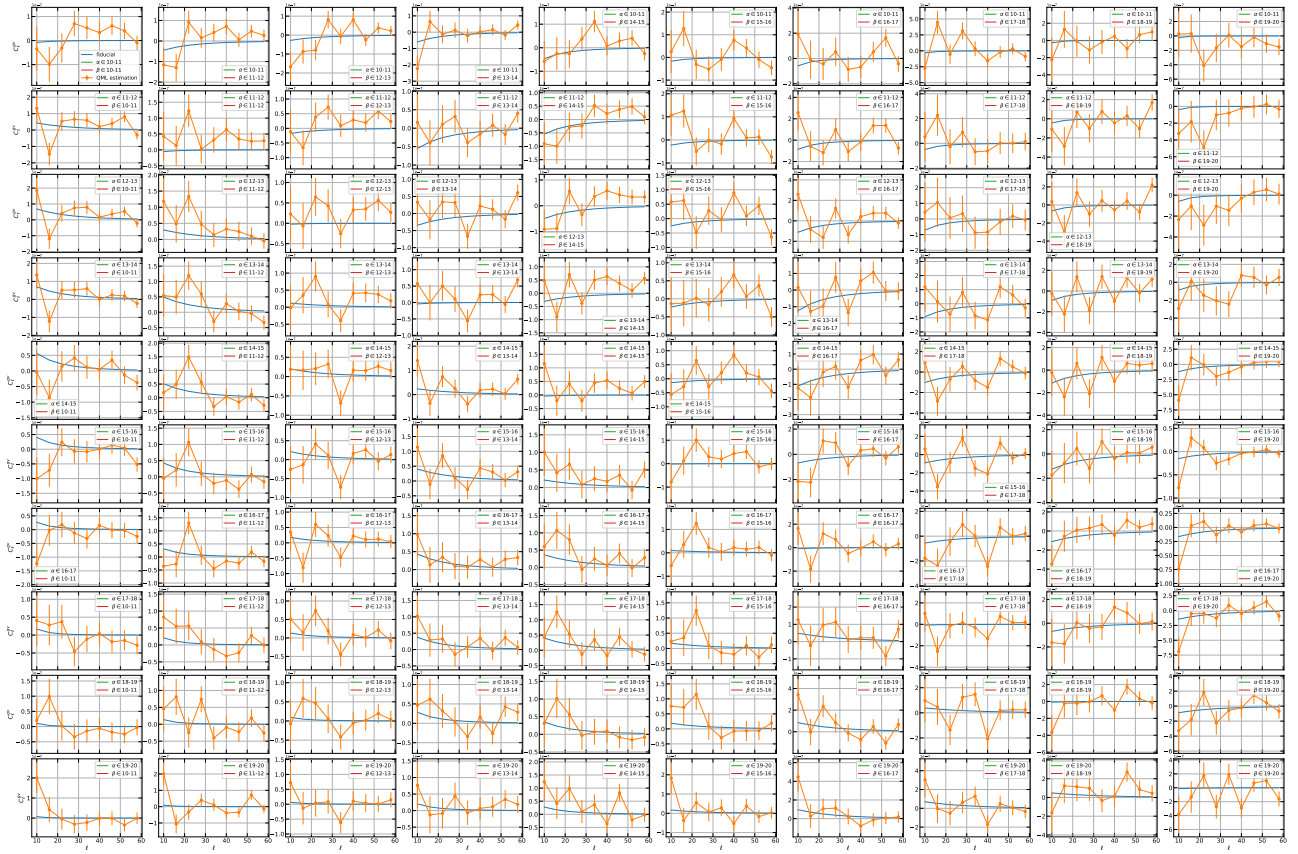


Figure 31: Same as Fig. 28 but with $\alpha \in 10 - 20, \beta \in 10 - 20$ block.